Experiments on an elliptic circulation control aerofoil

Drew A. Wetzel‡, John Griffin and Louis N. Cattafesta III†

Department of Mechanical and Aerospace Engineering, University of Florida,
Gainesville, FL 32611, USA

Experiments are performed on an elliptic circulation control aerofoil in an open-jet wind tunnel facility. The influence of blowing from a single trailing-edge slot on the external flow is assessed using two-component particle image velocimetry (PIV) and steady surface pressure measurements. The test section configuration (open jet or closed wall) significantly affects the leading-edge region of the flow field. PIV is also used to measure the curved wall jet and its interaction with the external flow near the trailing edge. PIV measurements of the curved wall jet reveal mean tangential velocity similarity in the outer region of the flow above the location where the tangential velocity reaches a local maximum. The length and velocity parameters required for similarity scale with the product of the chord Reynolds number and the momentum coefficient in accordance with the recent publication by Stalnov, Kribus & Seifert (*J. Renew. Sustain. Energy*, vol. 2, 2010, p. 063101). The separation location is also a function of the product of these parameters. The dataset is used to assemble equations to predict the similarity length scales, velocity scales and separation location. These equations compare well with the present measurements.

Key words: flow control, jets, wakes/jets

1. Introduction

Circulation control is a widely known method for augmenting forces on lifting surfaces. A circulation control aerofoil is generally equipped with a spanwise blowing slot that emits a high-momentum jet tangentially along a curved trailing edge. Relying on the Coanda effect, the jet entrains lower-momentum fluid from the free stream, delays separation, shifts the stagnation points, increases circulation and augments lift (Coanda 1938). While first applied to rotor craft, the use of circulation control has been proposed for a variety of applications, including vertical/short take-off and landing (V/STOL) aircraft (e.g. Antonov An-72 and An-74), automobiles, heat exchangers and wind turbines (Englar 1975, 2006; Day 2006; Gaeta, Englar & Blaylock 2006).

† Present address: Department of Mechanical Engineering, FAMU-FSU College of Engineering, Tallahassee, FL 32310, USA. Email address for correspondence: cattafesta@eng.fsu.edu

‡ Present address: The Boeing Company, P.O. Box 3707 MC 0R-JF, Seattle, WA 98124, USA.

The present investigation is concerned with the application of circulation control to underwater vehicles. Underwater vehicle manoeuvrability is limited by traditional control surfaces that generate lift forces proportional to the square of vehicle speed. Since the lift produced by circulation control is also related to the jet momentum, significant lift forces can be produced at any vehicle speed (or even at a standstill). Early experiments sought to optimize the geometry of a circulation control aerofoil, including the location and height of the blowing slot and the contour of the trailing edge (Kind & Maull 1968; Williams 1969; Williams & Howe 1970; Englar 1971; Abramson 1977). Later investigations proved the merits of a dual-slotted trailing-edge configuration, which not only doubles the operational lift range of the device but also permits significant lift augmentation with a small amount of blowing from the secondary slot (Abramson 2004; Rogers & Donnelly 2004). While circulation control technology is incredibly promising for underwater vehicles, there are numerous challenges that must be addressed prior to its implementation. One such concern is acoustics. Another is a sufficient understanding of the flow field to determine if flow similarity exists to any extent, which would greatly aid in the design and implementation of a circulation control system.

Recently, Howe (2002) considered the sound produced by a two-dimensional elliptic circulation control aerofoil in a high-Reynolds-number, low-Mach-number flow. Howe identified three prominent broadband noise sources: curvature noise, passive slot noise and slot–jet interaction noise. Curvature noise and passive slot noise are produced by the interaction of boundary-layer turbulence with the round trailing edge and slot lip, respectively. Slot–jet interaction noise is primarily generated when turbulence in the wall jet scatters off the slot lip. Howe's model relates these noise sources to a variety of mean flow parameters, including displacement thickness, mean velocity and friction velocity.

Detailed measurements of the trailing-edge flow field are therefore required to evaluate Howe's model in support of a parallel acoustic investigation, the results of which are presented by Wetzel, Liu & Cattafesta (2012). Furthermore, trailing-edge flow similarity is of equal importance, since flow similarity would permit the development of accurate flow predictions to support the design of circulation control aerofoils for many applications. To the authors' knowledge, the most comprehensive published experimental circulation control dataset is the laser Doppler velocimetry data of Novak & Cornelius (1986) and Novak, Cornelius & Roads (1987). There are also numerous studies on the curved wall jet, which is the primary mechanism exploited by circulation control. Various experimental studies in the absence of an external free stream have compared and contrasted curved wall jets with plane wall jet measurements and theory (Newman 1961; Wilson & Goldstein 1976; Kobayashi & Fujisawa 1983). Rew & Park (1988) investigated the flow of two opposing wall jets over a circular cylinder, similar to the trailing-edge geometry of a dual-slotted circulation control aerofoil. More recent investigations on curved wall jet flows, including their separation due to meandering streamwise vortices, include Neuendorf & Wygnanski (1999), Likhachev, Neuendorf & Wygnanski (2001), Neuendorf, Lourenco & Wygnanski (2004) and Han, de Zhou & Wygnanski (2006). The collection of curved wall jet studies has provided significant insight into the characteristics of the curved wall jet, albeit in quiescent surroundings. Indeed, in the absence of an external flow, wall jet flows have been shown to exhibit mean tangential velocity similarity when normalized using the maximum tangential velocity U_{max} and the normal distance from the surface where the outer region mean tangential velocity is $U_{max}/2$. However, we demonstrate herein that, with an external flow, the mean tangential velocity may never
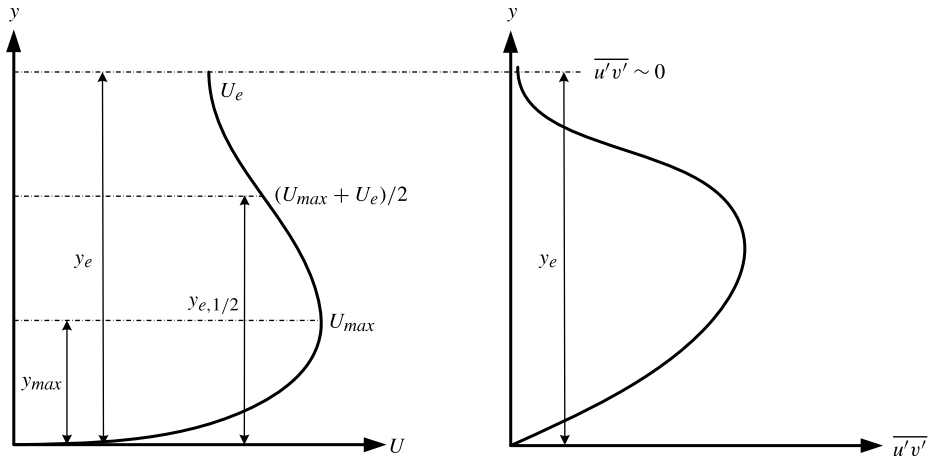
FIGURE 1. Length and velocity scales suggested by Launder & Rodi (1983).

decay to $U_{max}/2$. For such conditions, Launder & Rodi (1983) suggested the use of a defect velocity, defined as $U_{max} - U_e$, where U_e is the velocity where the Reynolds stress decays to a negligible value, and the length $y_{e,1/2}$, defined as the normal distance from the surface where the velocity is $(U_{max} + U_e)/2$. These scales are illustrated in figure 1. For a curved wall jet in an external flow, the mean tangential velocity is the only flow parameter known to exhibit similarity with these scales, and only the outer region of the flow has been shown to exhibit similarity (Novak & Cornelius 1986; Novak *et al.* 1987). Scaling based on turbulence parameters is not practicable for circulation control system design. We demonstrate that the outer region of the mean tangential velocity field can also be scaled using only mean flow parameters derived from the mean tangential velocity and mean shear profiles. Furthermore, we establish that the evolution of these mean flow length and velocity scales along the trailing-edge surface can be described as a function of the product of the chord Reynolds number and momentum coefficient, termed the Reynolds-corrected momentum coefficient by Stalnov, Kribus & Seifert (2010).

The present study is an experimental investigation of a circulation control aerofoil. Detailed measurements of the boundary-layer flow passing over the lip, the curved wall jet and the leading edge are obtained using high-resolution two-component particle image velocimetry (PIV). The experimental set-up, including the aerofoil, wind tunnel and test equipment, is described in § 2. The influence of circulation control on the free stream flow is addressed in § 3. It is shown that an open-jet test section, which is necessary for acoustic measurements, eliminates the leading-edge suction peak. More generally, the suction-side tunnel wall boundary condition is shown to significantly influence the leading-edge surface pressure distribution. Potential flow theory is used to explain this observed behaviour. The boundary layer passing over the slot lip – an important noise source according to Howe (2002) – is also measured with PIV and shown to remain unchanged when the test section is enclosed. The curved wall jet is the subject of § 4. A similarity solution is presented that prescribes the geometry required for complete flow similarity. Although the aerofoil under investigation does not meet these stipulations, the outer region of the mean tangential velocity field is found to exhibit similarity when normalized using length and velocity scales based on the maximum velocity and Reynolds stress, as suggested by Launder
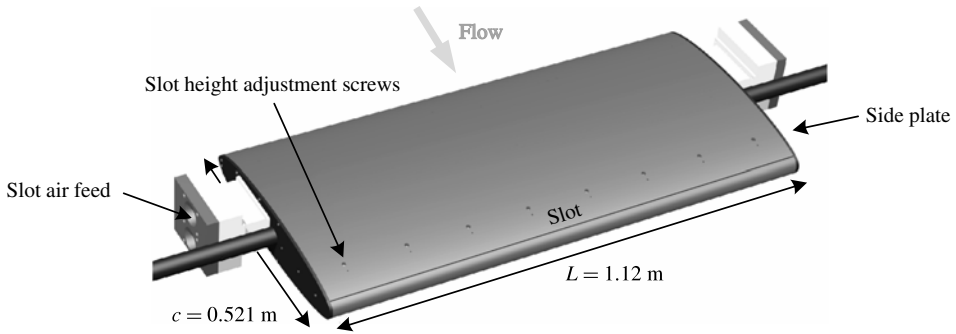
FIGURE 2. Circulation control aerofoil.

& Rodi (1983), and also the maximum velocity and mean shear as proposed by the present authors. These mean flow scales are measured for a variety of test conditions and found to collapse when scaled with the product of the chord Reynolds number and momentum coefficient. Equations for these scales are determined from the data and shown to agree well with measurements. Separation is then discussed in §5. Like the similarity scales examined in §4, the separation location is found to scale with the product of the chord Reynolds number and momentum coefficient. For the geometry of the present investigation, the separation location is predicted with high accuracy.

2. Experimental apparatus and instrumentation

2.1. *Circulation control aerofoil*

A two-dimensional, 20 % thickness-to-chord ratio elliptic circulation control aerofoil with a cylindrical trailing edge is used in this investigation. A schematic of the aerofoil is shown in figure 2. The geometry is based on the hydrofoil studied by Rogers & Donnelly (2004). The aerofoil has a 0.521 m chord and a 1.12 m wetted span. Dimensions of the dual-slotted trailing edge are provided in figure 3. Eight sets of push–pull screws evenly spaced across the span of the aerofoil provide slot height adjustment.

The aerofoil's hollow interior is divided into two independent air plenums that each supply a single blowing slot. Each plenum is provided with air from both ends of the aerofoil via 50.8 mm diameter supply hoses. Nylon constant-area air feeds, which are fabricated in a selective laser sintering machine, smoothly guide the pressurized air from the supply lines to the rectangular plenum inlets. To reduce internal flow speed, the inlet-to-slot area ratio is 4.7 for the nominal slot height, h, of 1.0 mm ($h/c = 0.0019$). Spanwise strips of porous ERG Duocel Aluminum Foam, 3.8 cm in total thickness, straighten the flow and attenuate contaminating air line noise. Adhesive-backed foam, 2 mm thick, is applied to all plenum surfaces, and Poly-fil polyester filling is packed in the plenum upstream of the aluminium foam for additional acoustic attenuation. The plenum is sealed using gaskets and various sealants.

Only a single blowing slot is used at any given time. The other unused blowing slot is set to the nominal 1.0 mm slot height and sealed with tape. The uniformity of the slot exit flow and the deflection of the lip above the blowing slot were assessed at this nominal slot height, which was measured using plastic shim stock. Constant-temperature hot-wire anemometry measurements along the slot centreline at
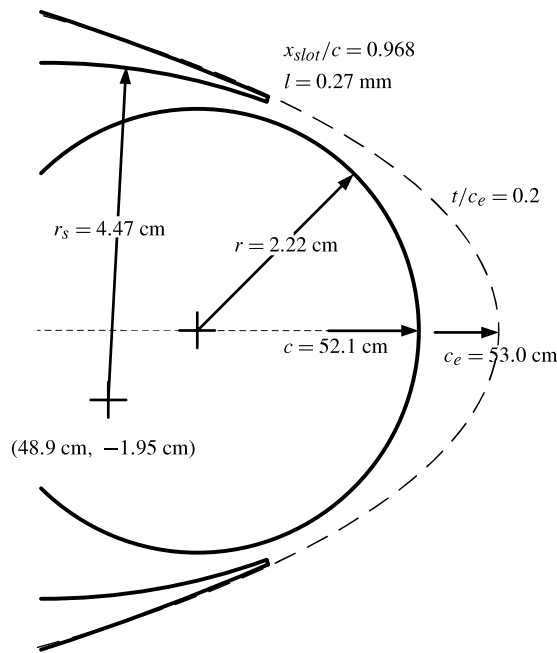
FIGURE 3. Aerofoil trailing-edge specifications: l is the lip thickness, r is the trailing-edge radius, t is the ellipse thickness, c is the aerofoil chord, c_e is the ellipse chord and r_s is the radius of the lip underside. The (x, y) coordinate origin is defined at the leading edge.

15 spanwise locations revealed that the centreline mean velocity varies by only 1.6 % at 41 m s^{-1} and 2.7 % at 87 m s^{-1} (Wetzel *et al.* 2010). Additionally, hot-wire spectra revealed the slot exit flow is turbulent if $Re_{jet} = hU_{jet}/\nu \geqslant 2600$ ($U_{jet} \geqslant 39$ m s^{-1} for $h/c = 0.0019$) (Wetzel 2011). A laser displacement sensor was used to measure lip displacement as a function of plenum pressure, which was incremented from atmospheric pressure to the maximum expected pressure during tunnel testing. The lip was found to deflect by less than 0.1 mm, or 8.8 %, at the maximum plenum pressure, and the greatest amplitude of vibration was less than 1×10^{-5} mm (Wetzel *et al.* 2010).

2.2. *Air delivery system*

A 1000 SCFM (standard cubic feet per minute; 28.3 normal m^3 min^{-1}), 300 hp (horsepower; 224 kW) compressor isolated from the anechoic test facility supplies desiccated, filtered and pressurized air to the plenums. The air is guided into the anechoic chamber via a 7.62 cm diameter air line at a flow rate regulated by a pneumatically operated 2.54 cm globe valve. Inside the chamber, the air line splits into four 3.81 cm diameter air lines, one for each plenum air feed. Each line includes a Lambda Square B-Plus 150 Venturi meter with a manual valve, a filter and a Universal Silencer U5-1-1/2 straight-through absorptive silencer for attenuating noise from the compressor motor and valve flow separation. An Omega PR-20 resistance temperature detector (RTD) is placed upstream of the branches to measure the stagnation temperature of the pressurized air. Flexible rubber hoses, 3.66 m long and 3.81 cm in diameter, connect the air lines to the aerofoil. A pressure relief valve is installed to prevent accidental plenum over-pressurization.

Slot jet velocity is estimated assuming an isentropic expansion from the plenum to the free stream,

$$U_{jet} = \left\{ 2RT_0 \left(\frac{\gamma}{\gamma - 1} \right) \left[1 - \left(\frac{p_\infty}{p_0} \right)^{(\gamma-1)/\gamma} \right] \right\}^{1/2}. \tag{2.1}$$

Here T_0 is the stagnation temperature measured by the RTD, p_0 is the plenum stagnation pressure measured using a pressure sensor connected to a tubulation installed in the plenum wall, and p_∞ is the static free stream pressure measured by the tunnel Pitot-static probe. Equation (2.1) is the standard used for estimating jet velocity in circulation control experiments, since it relies on p_∞ instead of the local surface pressure, and is often defined in the literature (e.g. Englar 1971; Abramson 1977). The ideal slot jet velocity estimates computed using (2.1) were found to compare reasonably well with (8–15 % less than) the centreline velocity measured using PIV (Wetzel *et al.* 2009). The influence of a non-zero plenum velocity on the jet velocity estimate was evaluated by Wetzel (2011) and, under the highest plenum velocity scenario, was found to produce an error of only 0.06 %.

The momentum coefficient is computed using

$$C_\mu = \frac{\dot{m} U_{jet}}{q_\infty S}, \tag{2.2}$$

where q_∞ is the dynamic pressure, S is the planform area of the lifting surface and the mass flow rate $\dot{m}$ is calculated from the product of the volumetric flow rate measured by the Venturi meters and the pressurized air density determined from the stagnation temperature and Venturi meter high-pressure port measurements.

2.3. *University of Florida Aeroacoustic Flow Facility*

The University of Florida Aeroacoustic Flow Facility (UFAFF) is an open-return wind tunnel with an open-jet test section installed in an ISO 3745-certified 100 Hz anechoic chamber. The test section measures 0.74 m × 1.12 m × 1.83 m in height, width and length in the flow direction, respectively. Test section speeds between 18 and 75 m s^{-1} can be reached with turbulent intensity levels below 0.1 % for frequencies 10 Hz and higher (Mathew *et al.* 2005). The circulation control aerofoil is installed 13 cm downstream of the nozzle exit at zero degrees geometric angle of attack. Strips of 12 mm wide, 0.4 mm thick Glasfaser Flugzeug-Service zig-zag turbulator tape are placed along the span of the aerofoil at 18 % chord to trip the upper and lower boundary layers. To maintain two-dimensional flow, the model is bounded on its sides by either 15.3 cm thick sound-absorbing foam or 5 mm thick polycarbonate sidewalls, the latter of which is employed for PIV. The top and bottom of the test section generally remain open to the anechoic chamber. However, the test section is closed to facilitate comparisons between open-jet and closed-wall experiments. Please refer to Mathew *et al.* (2005) for more information about the UFAFF.

2.4. *Surface pressure measurements*

Aerofoil surface pressure is measured at 39 midspan pressure ports using three 16-channel Esterline Pressure Systems pressure scanners (ranges 34.5, 6.89 and 2.49 kPa). The pressure scanners are also used to measure the Venturi meter pressure ports and the plenum pressure of the blowing slot. The measured surface pressure distribution is normalized and fitted with a cubic spline and then integrated to compute the lift
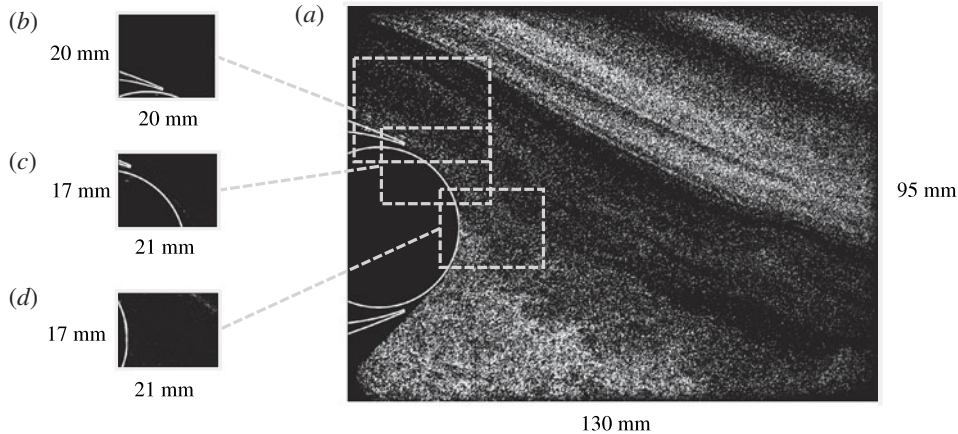
FIGURE 4. PIV trailing-edge measurement regions and image sizes: (*a*) trailing-edge wake, (*b*) flow over lip, (*c*) curved wall jet, and (*d*) curved wall jet separation. The aerofoil geometry is sketched for reference.

Region	Camera	Lens (mm)	Teleconverter	Freestream seeder	Jet seeder
Leading edge	LaVision	105	None	TSI 9307-6	—
Flow over lip	LaVision	200	None	TSI 9307-6	—
Curved wall jet	TSI	105	1.4, 2.0	TSI 9307-6	TSI 9302
Trailing-edge wake	TSI	60	None	Le Mautre CLF-4500	TSI 9302

TABLE 1. Summary of PIV image acquisition set-up, including camera (LaVision Imager Pro X 4M or TSI PowerView Plus 630157), camera optics and flow seeders.

coefficient. Uncertainty in surface pressure and lift are computed using the techniques described by Wetzel (2011).

2.5. *Particle image velocimetry*

PIV is used extensively in this investigation to study the influence of the wind tunnel open-jet test section on the flow field, the similarity of the curved wall jet flow and flow separation. A brief overview of these experimental set-ups is described in this section. More detailed information is provided by Wetzel (2011).

2.5.1. *Image acquisition*

The flow field is illuminated using a New Wave Research Solo 120XT Nd:YAG laser. The laser light passes through a spherical lens and a cylindrical lens to create a laser sheet. A mirror reflects the laser sheet onto the surface of the aerofoil at one of four regions of interest listed in table 1. The laser sheet is oriented in the chordwise plane for all experiments. A summary of the cameras and camera optics for each dataset are listed in table 1. Figure 4 illustrates the different regions of the trailing-edge flow field that are measured. The entire curved wall jet flow is captured in two separate sets of images labelled as figure 4(*c,d*). Between 500 and 1200 image pairs are acquired depending on the experiment and the quality of free stream flow seeding.
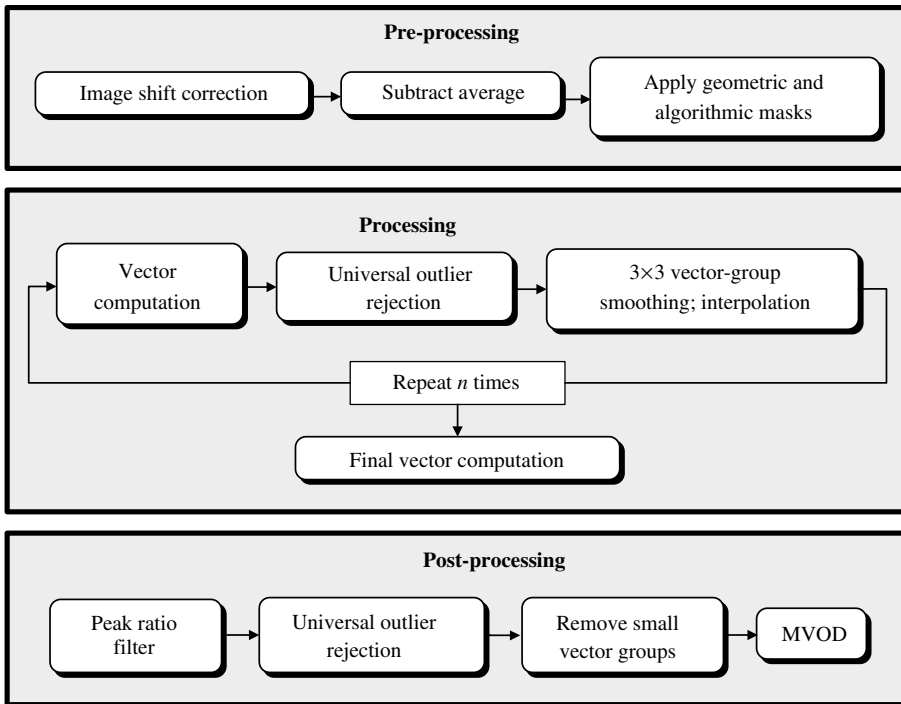
FIGURE 5. Vector computation steps.

Seeder	Particle diameter (μm)
Le Mautre CLF-4500	2–10
TSI 9307-6	1
TSI 9302	1

TABLE 2. Summary of flow seeders and particle diameter estimates.

The free stream is seeded using a variety of smoke machines and particle generators placed upstream of the wind tunnel inlet. A custom-built rake provides control of particle concentration and location by adjusting rake hole count and size. When measuring the curved wall jet flow, the trailing-edge blowing slot is also seeded. A small tube connected to a TSI 9302 atomizer is inserted into the plenum through the end of the model. The seeders used for each experiment are listed in table 1, and particle size estimates based on each seeder's specifications are provided in table 2. According to Melling (1997), a 1 μm particle has a 10 kHz frequency response in air.

2.5.2. *Vector computation*

Vectors are computed using LaVision DaVis 7.4 software (DaVis 2010). In general, images are processed following the steps outlined in figure 5. During the image pre-processing stage, each image pair is first shifted with respect to the first image to correct for camera vibration. Second, the image set average is subtracted from all images to improve particle clarity and reduce surface reflection. Finally, the aerofoil surface and regions of sparse seeding are masked.
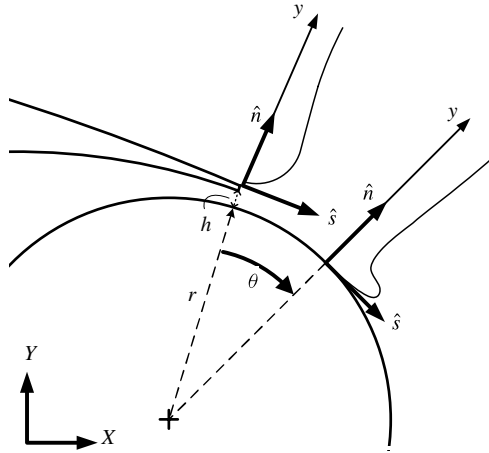
FIGURE 6. Coordinate systems and nomenclature at trailing edge.

Region	Initial window size (px)	Final window size (px)	Window overlap (%)	Resolution (mm vec^{-1})
Leading edge	64×64	32×32	50	0.95
Flow over lip	32×32	16×16	50	0.076
Curved wall jet	32×32	16×16	50	0.13
Trailing-edge wake	32×32	—	50	1.4

TABLE 3. Summary of processing parameters, including interrogation window sizes for the first two and last two passes, window overlap and final spatial resolution.

Vectors are computed using either a two- or four-iteration recursive cross-correlation processing scheme. Interrogation window size, overlap and final spatial resolution are given in table 3. For all datasets, a 1 : 1 Gaussian weighting function is applied to each window. Between each iteration, outliers are removed using the universal outlier detection technique developed by Westerweel (1994), a 3×3 vector group smoothing filter is applied and missing data are interpolated. Note that these steps are not performed after the final iteration. Instead, after the final iteration, outliers are rejected based on the value of the correlation peak ratio, Westerweel's universal outlier detection and the size of the surrounding vector group. Finally, in MATLAB, additional outliers are removed using the multivariate outlier detection (MVOD) approach described by Griffin *et al.* (2010). On average, fewer than 1 % of vectors are removed, and the highest number of vectors rejected for a given point is typically fewer than 20 %. Vectors are not interpolated or smoothed after the final iteration.

2.5.3. *Additional calculations*

After vectors are computed and outliers are removed, further processing is performed in MATLAB. Mean and turbulent flow quantities are computed in the local $\hat{s}$–$\hat{n}$ coordinate system defined at the lip edge and along the curved trailing edge, as shown in figure 6. For detailed information regarding the coordinate transformation, please refer to Wetzel (2011).

2.5.4. *Uncertainty*

A detailed uncertainty analysis is provided by Wetzel (2011) and summarized here. As noted previously, between 500 and 1200 image pairs are acquired for each case, depending on the experiment, to ensure an adequate number of samples for statistical convergence. The data are checked for convergence at particular points in the flow, and running averages of dimensionless velocity magnitude are found to converge within 95 % confidence intervals after no more than 150 samples.

Bias uncertainty is determined using the approach outlined by Coleman & Steele (2009) and applied to PIV data by Murray & Ukeiley (2007). The bias uncertainty in the magnitude of the velocity measurement is the root sum square of the uncertainty components associated with the pixel displacement, the measured lengths of the calibration target in physical units and pixels, and the time between exposures. The uncertainty in the direction of the velocity vector is a function of the pixel displacement and the bias uncertainty in the pixel displacement. Given the uncertainties in the velocity magnitude, direction and the coordinate transformation angle, bias uncertainties for the tangential and normal velocity components are found. Bias uncertainties in the turbulence intensity components $(\overline{u'^2})^{1/2}$ and $(\overline{v'^2})^{1/2}$ and Reynolds stress $\overline{u'v'}$ are dependent on the uncertainties associated with the instantaneous and mean tangential and normal velocity components.

Random uncertainty is estimated using the equations listed in table 1 of Benedict & Gould (1996). These random uncertainty estimates are valid regardless of the estimate distribution.

3. The global influence of circulation control

The flow field is characterized using a combination of static surface pressure and PIV measurements. The results from these tests are presented in this section.

3.1. *Surface pressure and lift characteristics*

Static surface pressure distributions are plotted in figure 7 for three different momentum coefficients, $C_\mu = 0$, 0.015 and 0.057 at $Re_c = 6.5 \times 10^5$ and $h/c = 0.0019$. For clarity, uncertainty bounds are not included, as they are smaller than the symbol size (typical 95 % confidence intervals are ± 0.006). The effect of blowing on the C_p distribution is apparent by the large trailing-edge suction peak whose magnitude increases substantially with larger values of C_μ. A leading-edge suction peak typically observed in circulation control aerofoil experiments, including those of Abramson (1975), is curiously absent. Furthermore, the lift produced by the aerofoil is substantially lower than the lift produced by Abramson's 20 % elliptic circulation control aerofoil (the chordwise slot location of Abramson's aerofoil matches the present investigation; there is no indication that a boundary-layer trip was used). Lift coefficients for a variety of momentum coefficients are compared in figure 8. It is possible that the absence of the leading-edge suction peak is the source of the lift deficiency observed in figure 8.

3.2. *Test section influence*

To determine if the aerofoil location in the test section is responsible for the missing leading-edge suction peak, the aerofoil position is varied by 13 cm ($0.25c$) vertically and by 38 cm ($0.73c$) in the streamwise direction. However, the C_p distributions remain unchanged. Since the tests performed by Abramson (1975) took place in a closed-wall wind tunnel, the absence of the leading-edge suction peak could be due
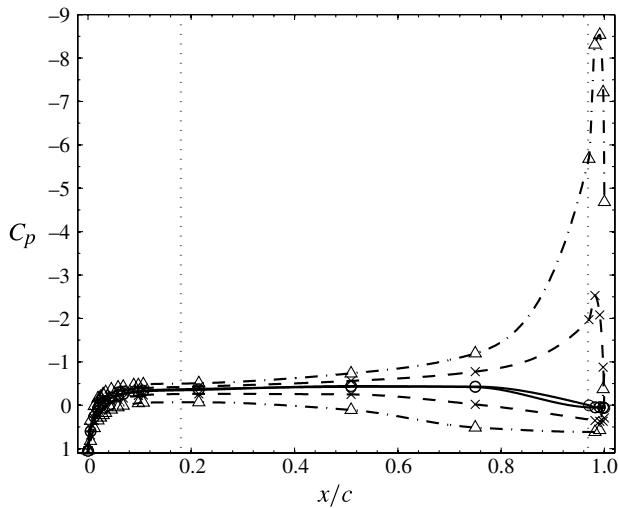
FIGURE 7. Aerofoil surface pressure (C_p), $Re_c = 6.5 \times 10^5$, $h/c = 0.0019$: —○—, $C_\mu = 0$ ($c_l = 0.010 \pm 0.04$); $- \times -$, $C_\mu = 0.015$ ($c_l = 0.58 \pm 0.04$); $-\cdot-\triangle-\cdot-$, $C_\mu = 0.057$ ($c_l = 1.5 \pm 0.04$). The left vertical dotted line represents the boundary-layer trip, and the right vertical dotted line corresponds to the slot.
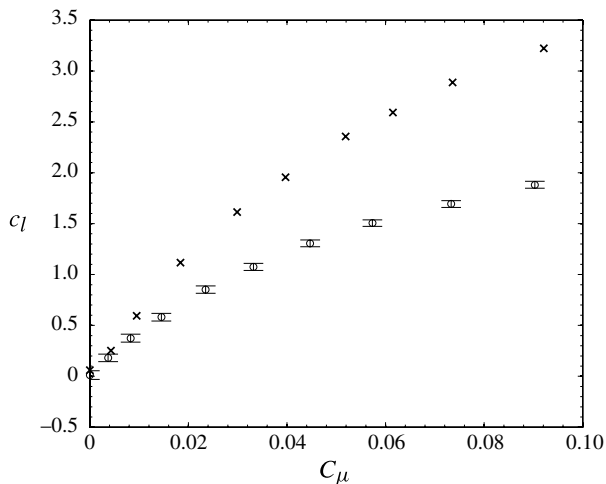

FIGURE 8. Lift coefficient (c_l) as a function of momentum coefficient, ○, present investigation $Re_c = 6.5 \times 10^5$, $h/c = 0.0019$; ×, Abramson (1975), 20 % elliptic circulation control aerofoil, $Re_c = 3.4 \times 10^5$, $h/c = 0.0013$.

to the UFAFF open-jet test section. To investigate this phenomenon further, the wind tunnel test section is enclosed with a foam ceiling and floor as shown in figure 9.

The C_p data measured in the closed-wall configuration are corrected to account for solid blockage (Pope & Rae 1984). Specifically, C_p, C_μ and Re_c are corrected using
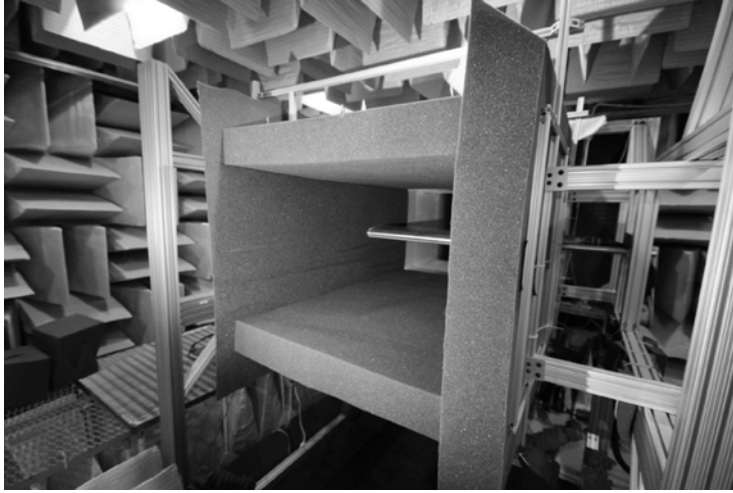
FIGURE 9. Photograph of UFAFF foam closed-wall test section.

the following equations:

$$C_{p,c} = \frac{C_p}{1 + 2\epsilon_t}, \tag{3.1}$$

$$C_{\mu,c} = \frac{C_\mu}{1 + 2\epsilon_t} \tag{3.2}$$

and

$$Re_{c,c} = Re_c(1 + \epsilon_t). \tag{3.3}$$

Here ϵ_t is one-quarter of the ratio between the model frontal area and the test section cross-sectional area and is equivalent to 0.0357. In the figures and discussion that follow, the subscript '$_{,c}$' is dropped for clarity.

Figure 10 compares midspan C_p distributions measured in both open-jet and closed-wall test sections for $C_\mu = 0$. Once again, for clarity, uncertainty bounds are not included, as they are typically smaller than the symbol size. Both C_p distributions have a similar shape, but the closed-wall C_p distribution is noticeably offset from its open-jet counterpart. Notably, the closed-wall C_p data are more negative, indicative of the increased flow speed caused by the addition of a floor and ceiling and their containment of the tunnel jet.

Figure 11 compares open-jet and closed-wall C_p distributions for $C_\mu = 0.057$. Both C_p distributions have similar prominent trailing-edge suction peaks associated with the trailing-edge jet. However, at the leading edge, the C_p distributions are drastically different. The leading-edge suction peak, absent in the open-jet test section configuration, appears when the test section is enclosed. Lift coefficients for the closed-wall and open-jet cases are compared with data from Abramson (1975) in figure 12. The closed-wall lift curve is in reasonable agreement with Abramson's lift values (Abramson applied the same blockage corrections as used in the present analysis). Therefore, the wind tunnel open jet is responsible for the disappearance of the leading-edge suction peak.
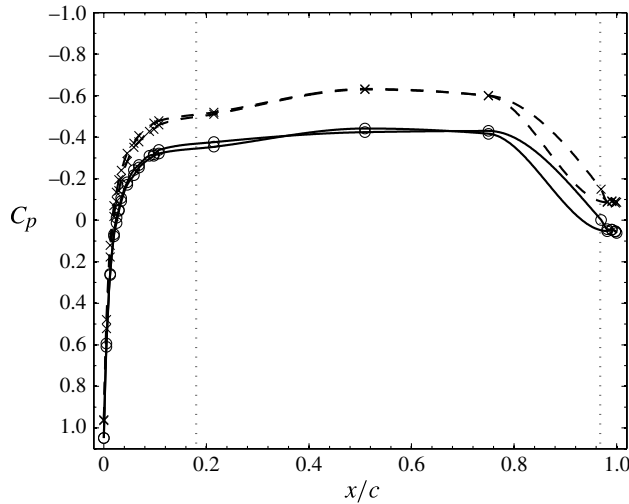
FIGURE 10. Aerofoil surface pressure (C_p), $C_\mu = 0$, $h/c = 0.0019$: —∘—, open-jet test section, $Re_c = 6.5 \times 10^5$; – –×– –, closed-wall test section, $Re_c = 6.7 \times 10^5$. The left vertical dotted line represents the boundary-layer trip, and the right vertical dotted line corresponds to the slot.
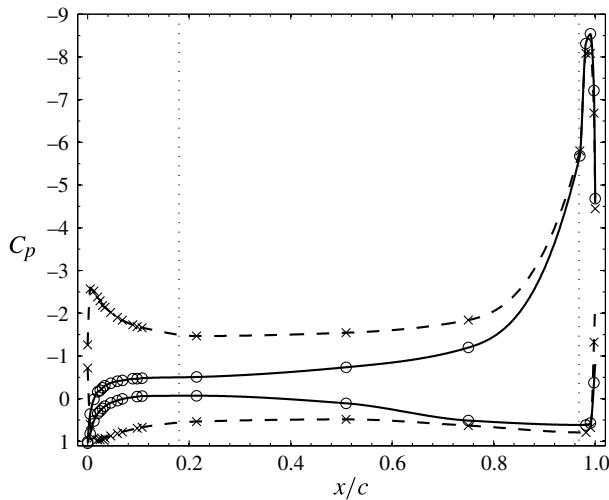

FIGURE 11. Aerofoil surface pressure (C_p), $h/c = 0.0019$: —∘—, open-jet test section, $C_\mu = 0.057$, $Re_c = 6.5 \times 10^5$ ($c_l = 1.5 \pm 0.04$); – –×– –, closed-wall test section, $C_\mu = 0.058$, $Re_c = 6.7 \times 10^5$ ($c_l = 2.7 \pm 0.03$). The left vertical dotted line represents the boundary-layer trip, and the right vertical dotted line corresponds to the slot.

Because this investigation is supporting a parallel effort to measure the noise produced by the circulation control aerofoil in the same open-jet facility, it is concerning that the C_p distributions measured with open-jet and closed-wall test sections differ significantly. Passive slot noise is theorized by Howe (2002) to be produced by free stream boundary-layer turbulence scattering off the slot lip. If the
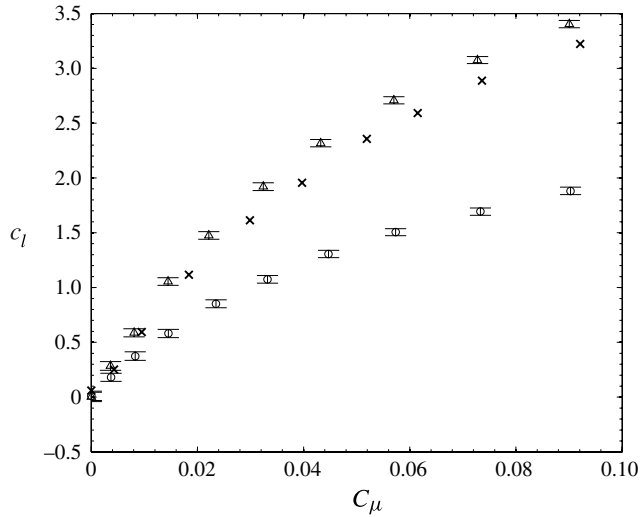
FIGURE 12. Lift coefficient (c_l) as a function of momentum coefficient, $\circ$, present investigation, open-jet test section, $Re_c = 6.5 \times 10^5$, $h/c = 0.0019$; $\triangle$, present investigation, closed-wall test section, $Re_c = 6.7 \times 10^5$, $h/c = 0.0019$; $\times$, Abramson (1975), 20 % elliptic circulation control aerofoil, $Re_c = 3.4 \times 10^5$, $h/c = 0.0013$.

characteristics of the turbulent boundary layer near the slot are highly dependent on the flow upstream of the slot, then so too in theory is the sound produced. PIV is used to further investigate the influence of the test section on the flow field, including the free stream boundary layer passing over the lip.

3.3. *Effect of closed-wall test section boundary conditions*

The leading-edge flow field and the boundary-layer flow passing over the slot lip are measured using PIV. In order to image the flow field, one foam sidewall is replaced with a clear polycarbonate panel. The PIV cameras are mounted behind this panel outside the flow. The foam ceiling is also replaced with a clear polycarbonate panel to permit the laser sheet to pass through and illuminate the flow. The other two tunnel walls remain foam. A picture of the test section enclosed for PIV measurements is provided in figure 13.

The laser sheet illuminates the flow only on the upper surface of the aerofoil (shadow regions are created below both the leading and trailing edges). Hence, the trailing-edge jet is emitted from the lower blowing slot, so the camera captures stagnation point movement on the upper surface of the leading edge. The flow passing over the slot lip is of interest as well, so tests are repeated with upper slot blowing, so the camera captures the flow above the upper surface lip. Thus, since the PIV experiments alternately utilize either upper or lower slot blowing, it is important to compare C_p distributions for both.

Figure 14 compares C_p distributions for upper and lower slot blowing in the two closed-wall test section configurations. Surprisingly, there are significant differences in the C_p distributions for upper and lower slot blowing when the test section is enclosed for PIV testing. With upper slot blowing (blowing on the same side as the polycarbonate ceiling), C_p values are more negative. Figure 14 also reveals that C_p data for lower slot blowing in the PIV test configuration (blowing on the same side

FIGURE 13. Photograph of closed-wall test section for PIV measurements. The foam ceiling and one foam wall are replaced with clear polycarbonate panels.
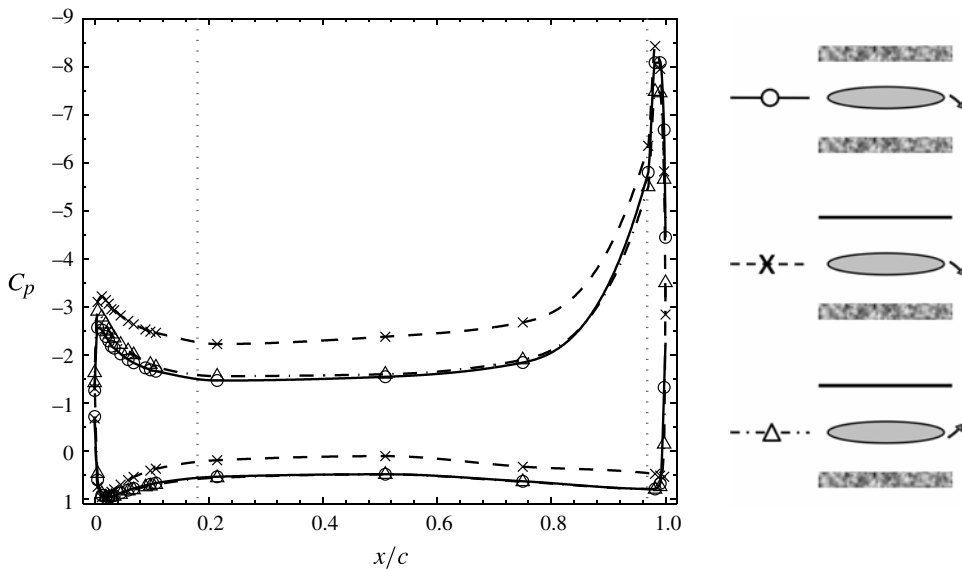

FIGURE 14. Aerofoil surface pressure (C_p) in closed-wall test sections, $Re_c = 6.7 \times 10^5$, $h/c = 0.0019$: —○—, foam ceiling and floor, upper slot blowing, $C_\mu = 0.058$ ($c_l = 2.7 \pm 0.03$); – –×– –, polycarbonate ceiling and foam floor, upper slot blowing, $C_\mu = 0.052$ ($c_l = 3.1 \pm 0.03$); –·–△–·–, polycarbonate ceiling and foam floor, lower slot blowing, $C_\mu = 0.053$ ($c_l = 2.8 \pm 0.03$). The left vertical dotted line represents the boundary-layer trip, and the right vertical dotted line corresponds to the slot.

as the foam floor) agree with the upper slot blowing C_p data obtained when the test section is enclosed with foam. Lower slot blowing experiments are not performed with the foam closed-wall test section.
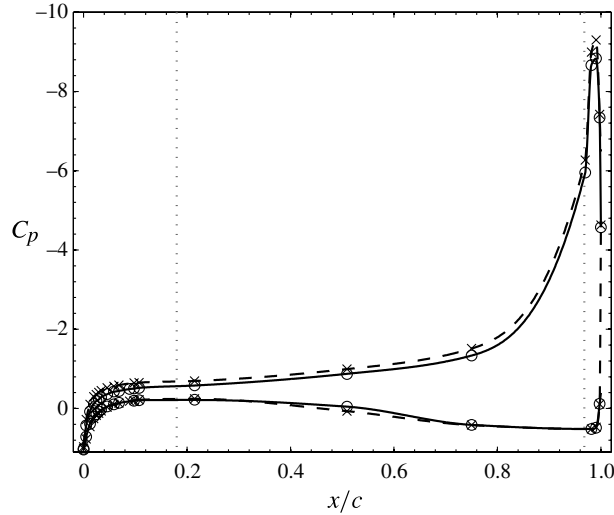
FIGURE 15. Aerofoil surface pressure (C_p) in open-jet test section, $Re_c = 6.5 \times 10^5$, $h/c = 0.0019$: —○—, upper slot blowing, $C_\mu = 0.057$ ($c_l = 1.5 \pm 0.04$); – –×– –, lower slot blowing, $C_\mu = 0.057$ ($c_l = 1.6 \pm 0.04$). The left vertical dotted line represents the boundary-layer trip, and the right vertical dotted line corresponds to the slot.

To rule out the blowing slots as the cause of these differences, C_p distributions for upper and lower slot blowing in the open-jet test section are compared in figure 15 for similar test conditions. The differences between the two distributions are minor compared to the observed differences in figure 14, and it is concluded that the variation in the C_p distributions in figure 14 is not the result of dissimilar blowing between the upper and lower slots. Instead, it appears that the boundary conditions imposed by the test section surface (polycarbonate versus foam versus air) on the same side as the blowing slot have a considerable influence on the flow field. A potential flow analysis is performed to provide insight into this observed flow behaviour.

3.4. *Potential flow analysis*

Potential flow theory is used to qualitatively determine the influence of the tunnel boundary conditions on the surface pressure distribution. Potential flow is useful in the study of circulation control, since viscous effects are minimal with sufficient blowing ($C_\mu \approx 0.002$ for the present aerofoil), and has been used extensively in past studies (Englar 1971; Abramson 1975; Rogers & Donnelly 2004). However, the analysis is qualitative since it cannot properly account for the trailing-edge wall jet and porous tunnel walls. The C_p distributions for potential lifting flow around a 20 % ellipse (analogous to upper-side circulation control blowing) in a variety of configurations are compared in figure 16 for a free stream $c_l = 1.90$. Specifically, the impact of a rigid, non-porous ground plane, ceiling plane and both ground and ceiling planes is assessed. The ground and ceiling planes are placed at the same distance from the ellipse, whose chord is identical to the aerofoil used in experiments, as the floor and ceiling installed in the UFAFF. Details regarding the potential flow analysis are located in the Appendix. Figure 16 reveals a few interesting details. First, the addition of a ceiling plane drastically augments the lift, whether or not a ground plane is present.
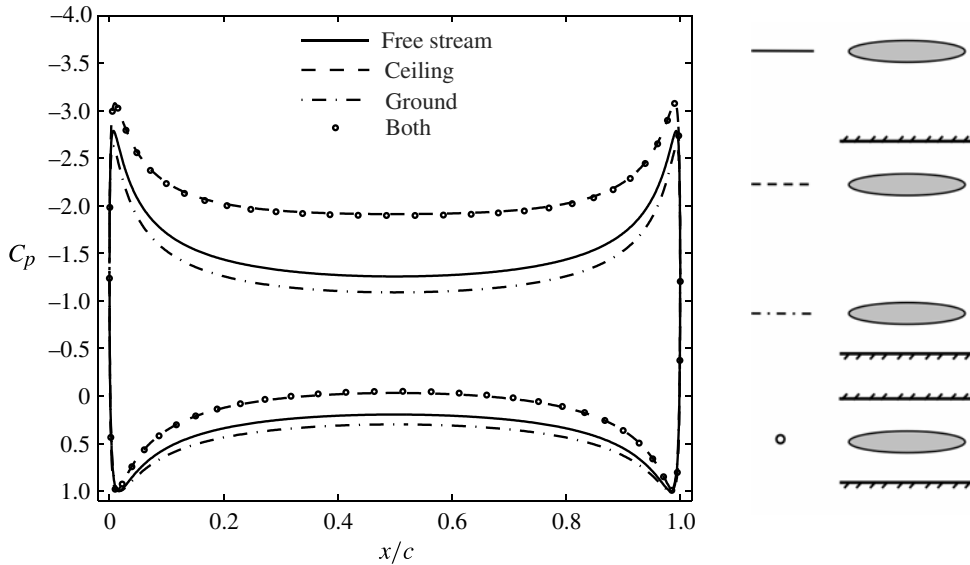
FIGURE 16. Potential lifting flow C_p on a 20 % ellipse (analogous to upper slot blowing), $U_\infty = 20$ m s^{-1}: ——, infinite free stream ($c_l = 1.9$); $- - -$, ceiling plane ($c_l = 2.3$); $-\cdot-\cdot-$, ground plane ($c_l = 1.8$); $\circ\,\circ$, ceiling and ground planes ($c_l = 2.3$).

Furthermore, the addition of a ground plane alone actually reduces the lift compared to the free stream case.

The potential flow analysis only assumes rigid, non-porous boundaries, whereas, in actual testing, a combination of impermeable (polycarbonate) and porous (foam) boundaries are used. For this reason, while the potential flow results cannot be expected to match experiments exactly, the qualitative trends revealed by figure 16 can still be applied to the measured observations. For example, figure 16 indicates that the presence of a rigid, non-porous (e.g. polycarbonate) plane on the same side as the blowing slot produces the greatest suction-side and lowest pressure-side C_p magnitudes, regardless of whether the opposite plane is present, absent, or, hence, porous (e.g. foam). This agrees with the measured data presented in figure 14, where the greatest suction-side and lowest pressure-side C_p magnitudes are observed when blowing is utilized on the same side as the polycarbonate tunnel ceiling. Additionally, figure 14 shows little variation in the measured C_p distributions when blowing is utilized on the same side as the porous foam ceiling and the pressure-side boundary is either polycarbonate or foam. This agrees with the theory in figure 16, which indicates that the inclusion of a ground plane has a minimal influence on the C_p distribution compared to the free stream and ceiling-only cases.

To further illustrate these trends, the potential flow solutions for the ellipse near a ground plane and ceiling plane alone are compared with closed-wall measurements. Since the potential flow solutions do not account for the presence of the trailing-edge jet and its contribution to the trailing-edge suction peak, measured and computed C_p distributions cannot be compared using equivalent lift coefficients. Instead, theoretical and measured distributions are compared by matching leading-edge stagnation points. Measured upper and lower slot blowing closed-wall C_p distributions (polycarbonate ceiling and foam floor) are compared to potential flow theory for a ceiling plane and
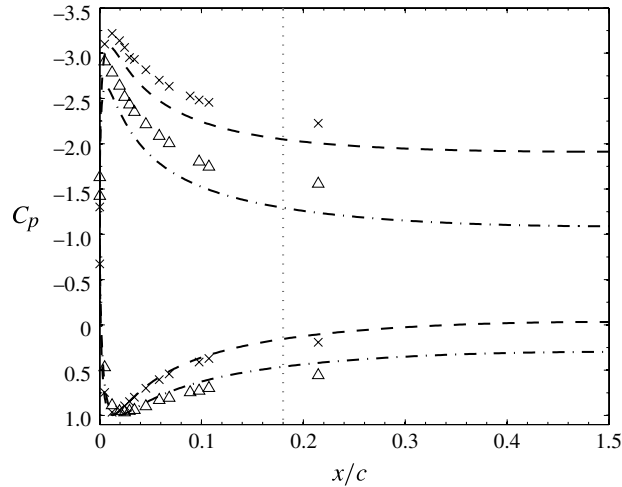
FIGURE 17. Aerofoil surface pressure (C_p) in closed-wall test section (polycarbonate ceiling and foam floor, $Re_c = 6.7 \times 10^5$, $h/c = 0.0019$) compared with potential flow theory: $\times$, upper slot blowing, $C_\mu = 0.052$ ($c_l = 3.1 \pm 0.03$); $\triangle$, lower slot blowing, $C_\mu = 0.053$ ($c_l = 2.8 \pm 0.03$); $- - -$, potential flow, ceiling plane ($c_l = 2.3$); $- \cdot - \cdot -$, potential flow, ground plane ($c_l = 1.8$).

ground plane, respectively, in figure 17. The measured leading-edge stagnation points are found to match with theory for both datasets when the infinite free stream lift coefficient is 1.90. At the leading edge, the theory agrees well with the measurements, and the trends revealed by figure 16 are clearly followed by the measured data.

Varying the tunnel blockage ratio, computed from the ratio of the aerofoil thickness to tunnel height, in the potential flow analysis reveals that the differences between the computed closed-wall test section and free stream surface pressure distributions are insignificant when the tunnel blockage ratio is less than 6 %. By comparison, the tunnel blockage ratio for the present investigation is 14 %, and the blockage ratios for the studies by Abramson (1975) and Novak & Cornelius (1986) were 8 and 7 %, respectively.

In summary, the potential flow analysis and measured C_p datasets support the following conclusions regarding the surface pressure measurements. (i) The leading-edge suction peak that appears when the test section is enclosed is caused by a suction-side boundary (e.g. tunnel ceiling) blockage effect. (ii) The porosity of the suction-side boundary is important. Circulation and lift are further enhanced as the boundary approaches zero porosity. Hence, as the measurements indicate, a non-porous (polycarbonate) suction-side boundary augments lift compared to a porous foam suction-side boundary. (iii) The absence, presence, or porosity of a pressure-side boundary is nearly irrelevant, especially in addition to a suction-side boundary. (iv) Lastly, the tunnel blockage ratio plays a significant role in the leading-edge suction peak pressures and should be less than 6 % to accurately reproduce free stream surface pressures.

3.5. *PIV results*

Theory and measurements agree that there are significant differences in the C_p distributions depending on the suction-side boundary condition. Enclosing the test
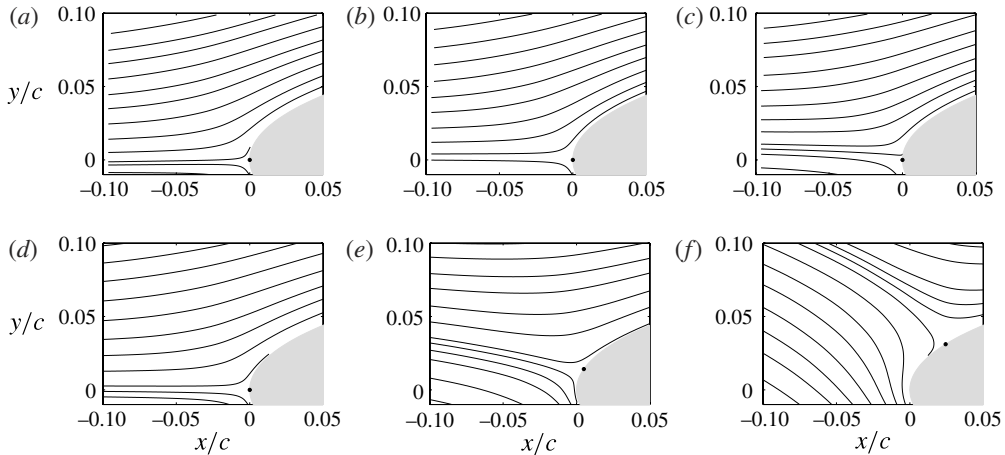
FIGURE 18. Leading-edge mean flow streamlines in (*a–c*) open-jet test section, $Re_c = 6.5 \times 10^5$, and (*d–f*) closed-wall test section, $Re_c = 6.7 \times 10^5$. Flow is from left to right, and the origin is located at the leading edge. Lower slot blowing is used for all cases, $h/c = 0.0019$; (*a*) $C_\mu = 0$, (*b*) $C_\mu = 0.014$, (*c*) $C_\mu = 0.057$, (*d*) $C_\mu = 0$, (*e*) $C_\mu = 0.013$, (*f*) $C_\mu = 0.053$. The black circles represent the leading-edge stagnation point measured by the steady surface pressure ports.

section clearly produces the leading-edge suction peak absent in the open-jet test section measurements. The influence of enclosing the test section on the leading-edge flow is also captured by PIV. Mean flow streamlines for both open-jet and closed-wall test section configurations at a variety of lower blowing slot momentum coefficients are shown in figure 18. The leading-edge stagnation points measured by the steady surface pressure ports are indicated by black circles in the plots. In the open-jet test section configuration, leading-edge stagnation point movement and streamline curvature are minimal as C_μ increases. Conversely, when the test section is enclosed, the leading-edge stagnation point moves considerably with increasing C_μ, and streamline curvature is greatly enhanced.

As discussed in the Introduction, this study is supporting an effort to evaluate the noise prediction model of Howe (2002). Passive slot noise is theorized by Howe to be produced by turbulence in the free stream boundary layer scattering off the slot lip. If the characteristics of the turbulent boundary layer near the slot vary with test section configuration, then, according to the theory, so does the sound produced. The turbulent boundary layer passing over the slot lip is measured using PIV in both open-jet and closed-wall tunnel configurations for a variety of upper slot blowing momentum coefficients. The results are presented in figures 19–21. Profiles of mean tangential and normal velocities, turbulence intensities and Reynolds stress are plotted. For clarity, only every fourth data point is displayed, and solid lines represent uncertainty bounds. Reliable data are measured within 0.12 mm of the aerofoil surface. Without blowing (figure 19), the profiles are normalized using the local free stream velocity and the boundary-layer thickness (open-jet test section, $\delta = 10.9$ mm; closed-wall test section, $\delta = 10.6$ mm). With blowing (figures 20 and 21), the mean tangential velocity profiles appear more like wall jet profiles, and the local maximum velocity and the boundary-layer thickness based on where $\bar{U} = 0.99U_{max}$ are used to normalize the data (open-jet test section, $\delta = 4.6$ mm ($C_\mu = 0.014$), $\delta = 2.1$ mm ($C_\mu = 0.057$); closed-wall test
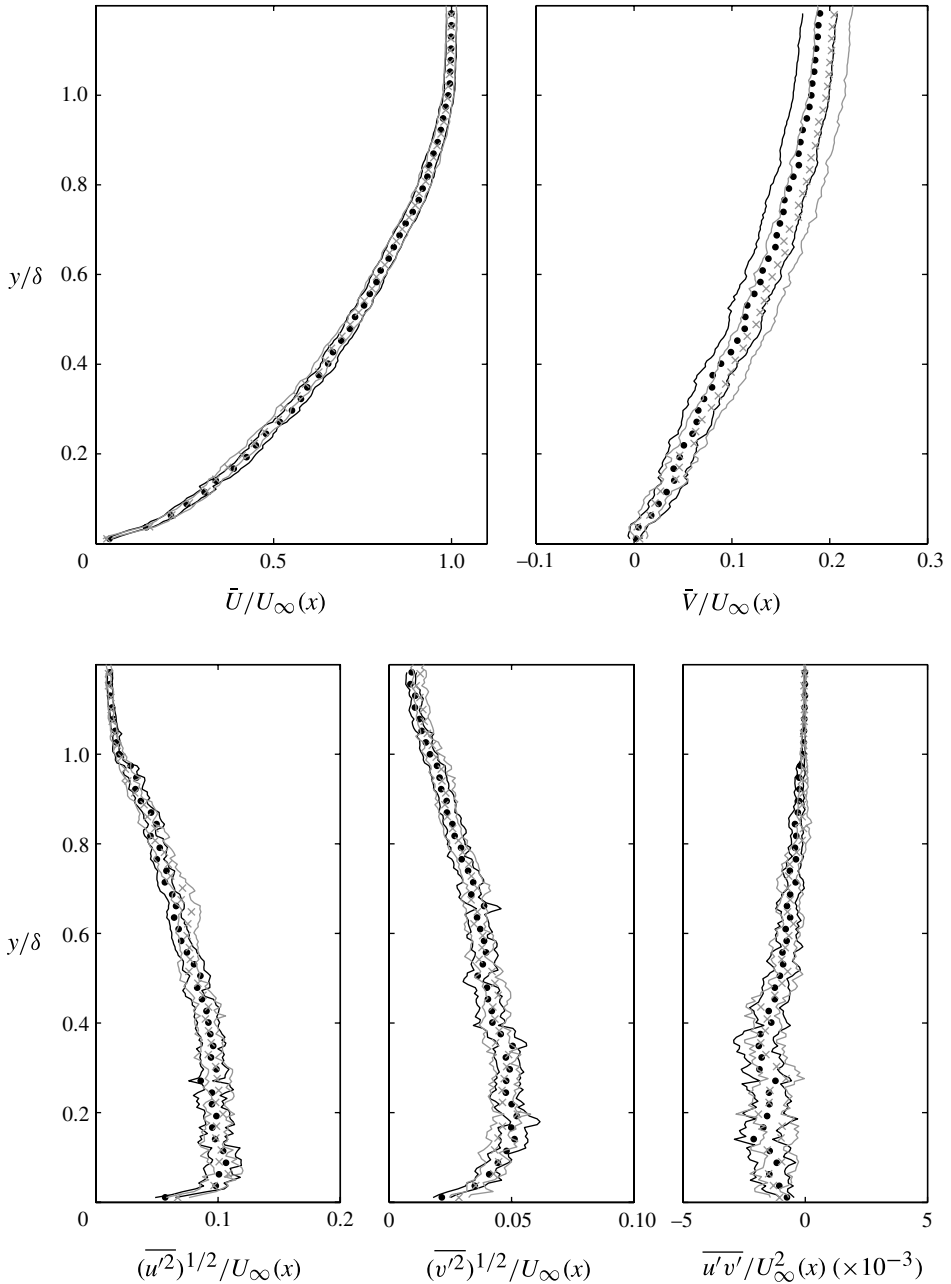
FIGURE 19. Comparison of profiles at the lip edge, $C_\mu = 0$: ●, open-jet test section, $Re_c = 6.5 \times 10^5$; ×, closed-wall test section, $Re_c = 6.7 \times 10^6$. The slot height is $h/c = 0.0019$ for both cases. For clarity, only every fourth data point is displayed. Solid lines represent uncertainty bounds.

FIGURE 20. Comparison of profiles at the lip edge: $\bullet$, open-jet test section, $Re_c = 6.5 \times 10^5$, $C_\mu = 0.014$; $\times$, closed-wall test section, $Re_c = 6.7 \times 10^6$, $C_\mu = 0.013$. The slot height is $h/c = 0.0019$ for both cases. For clarity, only every fourth data point is displayed. Solid lines represent uncertainty bounds.
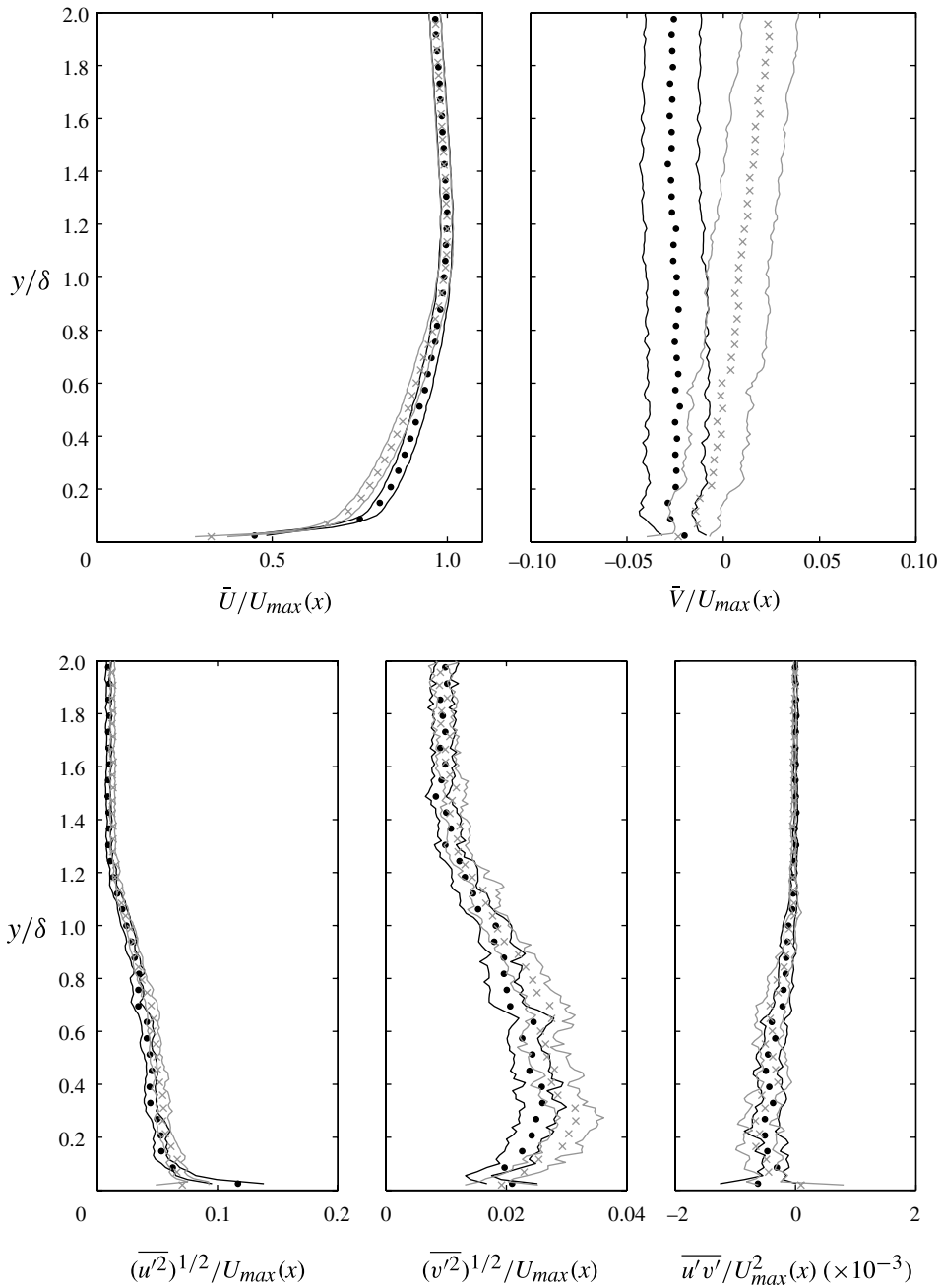
FIGURE 21. Comparison of profiles at the lip edge: ●, open-jet test section, $Re_c = 6.5 \times 10^5$, $C_\mu = 0.057$; ×, closed-wall test section, $Re_c = 6.7 \times 10^6$, $C_\mu = 0.053$. The slot height is $h/c = 0.0019$ for both cases. For clarity, only every fourth data point is displayed. Solid lines represent uncertainty bounds.
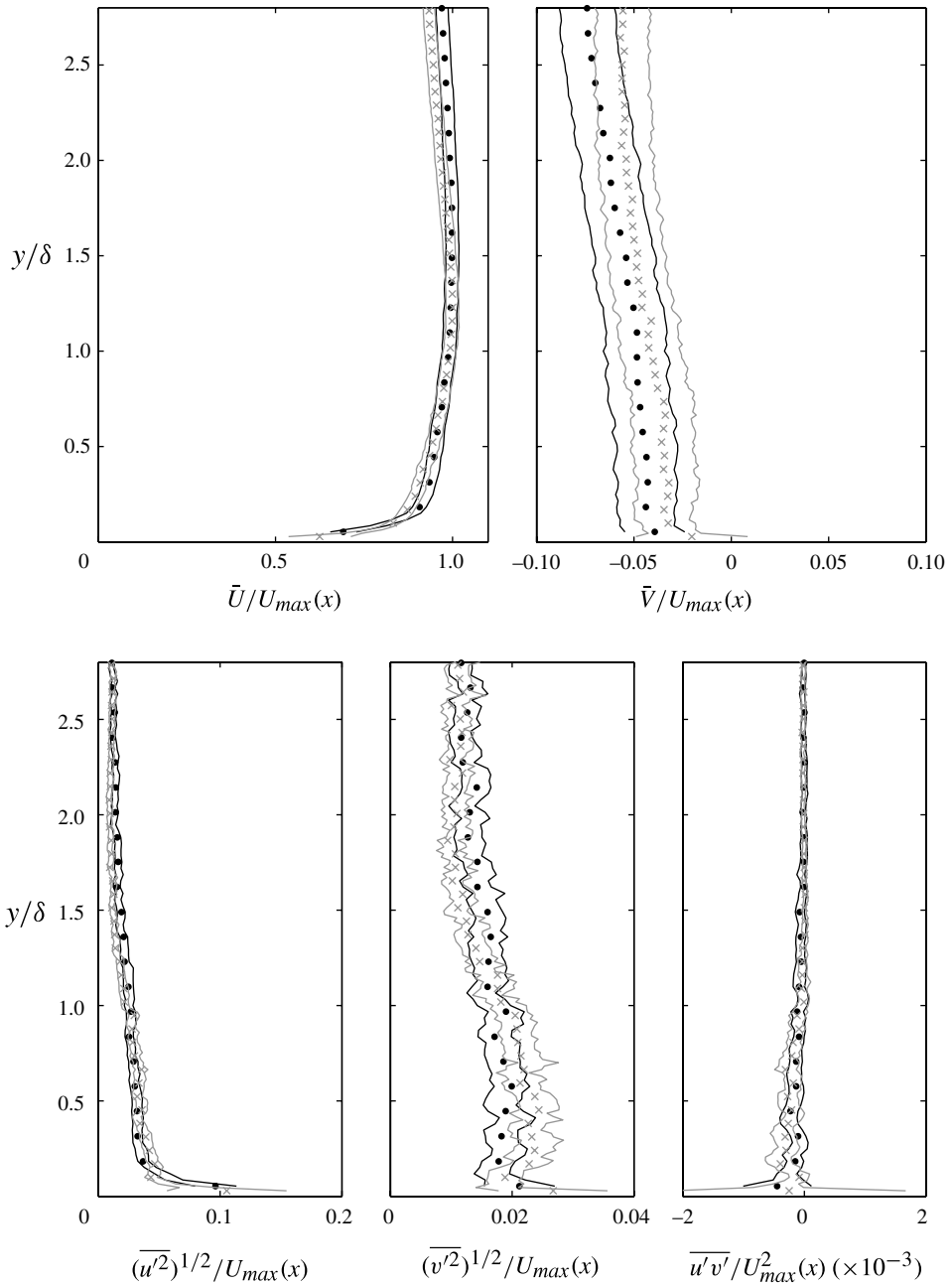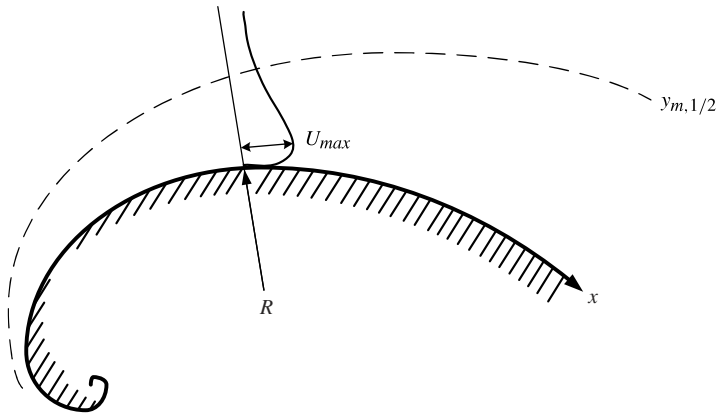
FIGURE 22. Logarithmic spiral surface (reproduced from Guitton & Newman (1977)).

section, $\delta = 5.8$ mm ($C_\mu = 0.014$), $\delta = 4.0$ mm ($C_\mu = 0.057$)). For all cases, there are minor differences between the profiles, and these deviations are typically within the measurement uncertainty. Hence, based on Howe's (2002) model of circulation control noise, the sound produced by the interaction of the turbulent boundary layer with the slot lip should be the same whether or not the test section is opened or closed.

4. Characteristics of the circulation control curved wall jet

The primary mechanism exploited by circulation control is the curved wall jet, which is expected to play an important role in the production of circulation control noise. Curvature noise is theorized by Howe (2002) to be produced by the interaction of boundary-layer turbulence with the rounded trailing edge. The displacement thickness, local mean velocity and friction velocity – the parameters required to assess Howe's model – are clearly dictated by the interaction of the curved wall jet with the external flow. Thus, there is a need for high-resolution flow measurements of the curved wall jet to determine these parameters. Of similar importance and interest, however, is the potential for flow similarity. If the circulation control wall jet exhibits similarity, then it may be possible to predict the evolution of the flow and its various length and velocity scales. Such a finding would have direct application to Howe's model and also the design of circulation control aerofoils for a variety of applications.

Unfortunately, the literature provides evidence that full flow similarity may only be possible for very specific geometries. Guitton & Newman (1977) presented a similarity solution for a curved wall jet in quiescent surroundings and concluded that full flow similarity is only possible if the trailing-edge surface is defined by a logarithmic spiral, e.g. $r \propto e^{R\theta/x}$ in polar coordinates (r, θ), where R is the local radius of curvature, x is the arc length from the origin and R/x is a constant that defines the tightness of the spiral. A logarithmic spiral is illustrated in figure 22. Their analysis is extended in the next section for the curved wall jet in an external flow.

4.1. *General similarity solution*

Using the turbulent forms of the governing equations in polar coordinates, Guitton & Newman (1977) developed a similarity solution for a curved wall jet in the absence of

Parameter	Scaling
R	x
$y_{1/2m}$	x
U_{max}	x^a

TABLE 4. Scaling of length and velocity parameters from similarity solution of Guitton & Newman (1977); x is the arc length and a is a constant.

external flow assuming the following forms of the similarity functions f, g and g_{12}:

$$u = U_{max} f'(\eta), \tag{4.1}$$

$$-\overline{u'v'} = U_{max}^2 g_{12}(\eta), \tag{4.2}$$

$$\overline{u'^2} - \overline{v'^2} = U_{max}^2 g(\eta), \tag{4.3}$$

$$\eta = \frac{y}{y_{1/2m}}. \tag{4.4}$$

Here U_{max} is the local maximum tangential velocity, and $y_{1/2m}$ is the local normal distance from the surface, where $\bar{U} = U_{max}/2$ in the outer region. Guitton & Newman (1977) showed that the wall jet flow is only self-similar provided the surface is defined by a logarithmic spiral, $r \propto e^{R\theta/x}$. The constant ratio x/R dictates the rate at which the local radius of curvature, R, grows. The larger the value of x/R, the larger the local radius of curvature at some arc length x. Table 4 lists the relevant length and velocity parameters and how each scales with arc length x.

Compared to the simpler curved wall jet issuing into a quiescent fluid, the velocity of a curved wall jet with an external flow may never decay to $U_{max}/2$. For such conditions, Launder & Rodi (1983) suggested the use of a defect velocity, $U_{max} - U_e$, where U_e is the tangential velocity where the Reynolds stress decays to a negligible value, and the length scale $y_{e,1/2}$, defined as the normal distance from the surface where $\bar{U} = (U_{max} + U_e)/2$ in the outer region. These scales are illustrated in figure 1. The similarity analysis of Guitton & Newman (1977) is extended for a curved wall jet in the presence of an external flow by assuming the following forms of the similarity functions:

$$u = U_1 f'(\eta) + U_2, \tag{4.5}$$

$$-\overline{u'v'} = U_1^2 g_{12}(\eta), \tag{4.6}$$

$$\overline{u'^2} - \overline{v'^2} = U_1^2 g(\eta), \tag{4.7}$$

$$\eta = \frac{y - y_2}{y_1}. \tag{4.8}$$

If the scales suggested by Launder & Rodi (1983) are applied to these functions, then $U_1 = U_{max} - U_e$, $U_2 = U_e$, $y_1 = y_{e,1/2} - y_{max}$ and $y_2 = y_{max}$.

The remainder of the similarity analysis follows the same steps as outlined by Guitton & Newman (1977) and is included in detail in Wetzel (2011). The resulting

similarity equation is

$$\boxed{\frac{y_1}{U_1}\frac{\mathrm{d}U_1}{\mathrm{d}x}(f'^2 - f''f + 2g)} - \boxed{\frac{\mathrm{d}y_1}{\mathrm{d}x}(f''f + \eta g')} - \boxed{g'_{12}}$$

$$-\boxed{\frac{y_1}{R}}\left(\boxed{\frac{y_1}{U_1}\frac{\mathrm{d}U_1}{\mathrm{d}x}}[A] + \boxed{\frac{\mathrm{d}y_1}{\mathrm{d}x}}[B] + \boxed{(\eta g'_{12} + 2g_{12})} + \frac{y_1}{U_1}\frac{\mathrm{d}U_2}{\mathrm{d}x}[C] + \frac{\mathrm{d}y_2}{\mathrm{d}x}[D]\right)$$

$$+\frac{y_1}{U_1}\frac{\mathrm{d}U_2}{\mathrm{d}x}(f' - \eta f'') - \frac{\mathrm{d}y_1}{\mathrm{d}x}\frac{U_2}{U_1}(\eta f'') + \frac{\mathrm{d}y_2}{\mathrm{d}x}\left[\frac{U_2}{U_1}(f'') - g'\right]$$

$$+\frac{y_1}{U_1}\frac{U_2}{U_1}\left[\frac{\mathrm{d}U_1}{\mathrm{d}x}(f') + \frac{\mathrm{d}U_2}{\mathrm{d}x}\right] - \frac{y_2}{R}(g'_{12}) = 0, \tag{4.9}$$

where

$$A = \boxed{\left(f'f + 2\int_\eta^\infty f'^2\,\mathrm{d}\eta\right)} + \frac{U_2}{U_1}\left(f + 4\int_\eta^\infty f'\,\mathrm{d}\eta\right) + 2\int_\eta^\infty\left(\frac{U_2}{U_1}\right)^2\mathrm{d}\eta, \tag{4.10}$$

$$B = \boxed{\left(f'f + \int_\eta^\infty f'^2\,\mathrm{d}\eta\right)} + \frac{U_2}{U_1}\left(f + \eta f' + 2\int_\eta^\infty f'\,\mathrm{d}\eta\right) - \eta\left(\frac{U_2}{U_1}\right)^2 + \int_\eta^\infty\left(\frac{U_2}{U_1}\right)^2\mathrm{d}\eta, \tag{4.11}$$

$$C = (\eta f') + \frac{U_2}{U_1}\eta, \tag{4.12}$$

$$D = \frac{U_2}{U_1}(f') - \frac{U_2^2}{U_1^2}. \tag{4.13}$$

The boxed terms comprise Guitton & Newman's (1977) original similarity solution. When $U_2 = 0$ and $y_2 = 0$, such that the similarity functions take the form $u = U_1 f'(\eta)$ and $\eta = y/y_1$, only the boxed terms remain (to match Guitton and Newman's original similarity solution exactly, $y_1 = y_{max}$ and $U_1 = U_{max}$).

For similarity, all terms outside the parentheses in (4.9) must be constant. Consider the term

$$\frac{\mathrm{d}y_1}{\mathrm{d}x}(f''f + \eta g'). \tag{4.14}$$

Since $\mathrm{d}y_1/\mathrm{d}x$ must be independent of x, it follows that $y_1 \propto x$. Similarly, note the term

$$\frac{y_1}{R}(\eta g'_{12} + 2g_{12}). \tag{4.15}$$

Since y_1/R must be independent of x, then $R \propto y_1 \propto x$. Therefore, in order for true similarity to be achieved, the surface must be a logarithmic spiral, i.e. $r \propto e^{R\theta/x}$, where R is the local radius of curvature labelled in figure 22. Table 5 lists the length and velocity parameters from this analysis and how each scales with arc length x.

Since the trailing edge of the circulation control aerofoil under investigation has a constant radius, exact self-similarity of the flow cannot be achieved. A logarithmic spiral trailing edge is not practicable for underwater vehicle applications where control surface symmetry is desired as illustrated by figure 23 (if a portion of the logarithmic spiral trailing edge is mirrored about the chord line to ensure symmetry, then a discontinuity would result at $x/c = 1$). In addition, a logarithmic spiral design would
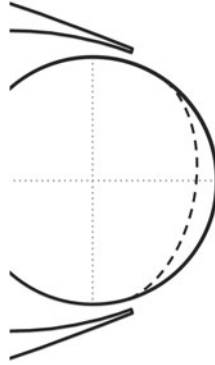
FIGURE 23. Circular (solid) and logarithmic spiral (dashed) trailing edges. A logarithmic spiral trailing edge is asymmetric about the chord line, making this configuration impracticable for underwater vehicles.

Parameter	Scaling
R	x
y_1	x
y_2	x
U_1	x^a
U_2	x^a
U_2/U_1	Constant

TABLE 5. Scaling of length and velocity parameters from general similarity solution of a curved wall jet in an external flow; x is the arc length and a is a constant.

interfere with the secondary blowing slot used to control excessive jet attachment at extremely high primary blowing slot momentum coefficients (Rogers & Donnelly 2004).

Although flow similarity is not possible over the entire trailing edge, even partial flow similarity could still prove useful for circulation control design purposes. Before the curved wall jet flow is examined for similarity, dimensional analysis is used to identify dependent parameters.

4.2. *Dimensional analysis*

A dimensional analysis is performed to determine the important dimensionless parameters associated with the trailing-edge flow field (Panton 2005). As an example, y_{max}, the normal distance from the surface where $\bar{U} = U_{max}$, is used as the relevant dependent length scale. Any other dependent length or velocity scale could be used in its place.

First, all significant parameters in the problem are identified. Note that the flow is assumed to be incompressible, since $M_{jet} < 0.3$ for all cases considered, and steady. The geometric properties include the chord c, slot height h, circular trailing-edge radius r and lip thickness l. Of these, the chord, trailing-edge radius and lip thickness are fixed in the current experimental investigation. Flow properties include density ρ, viscosity μ, free stream velocity U_∞, jet velocity U_{jet} and y_{max}. There are nine total dimensional variables.

Case	h/c ($\times 10^{-3}$)	Re_c ($\times 10^5$)	U_∞ (m s^{-1})	U_{jet} (m s^{-1})	U_{jet}/U_∞	C_μ
1	1.9	6.5	20	20	1	0.0039
2	1.9	6.5	20	40	2	0.015
3	1.9	6.5	20	80	4	0.057
4	1.9	6.5	20	38	1.9	0.014
5	1.9	13	40	78	2.0	0.014
6	2.9	6.5	20	32	1.6	0.014
7	2.9	13	40	64	1.6	0.014

TABLE 6. Test cases presented.

Three repeating parameters are required since the units of time, mass and length are represented. If c, U_∞ and ρ are chosen as the repeating parameters, the six Π groups are: $\Pi_1 = h/c$, $\Pi_2 = r/c$, $\Pi_3 = l/c$, $\Pi_4 = \rho U_\infty c/\mu = Re_c$, $\Pi_5 = U_{jet}/U_\infty$ and $\Pi_6 = y_{max}/c$. The fifth of these, Π_5, is recast into the momentum coefficient:

$$\Pi_5' = 2\Pi_1(\Pi_5)^2 = 2\left(\frac{h}{c}\right)\left(\frac{U_{jet}}{U_\infty}\right)^2 = C_\mu. \tag{4.16}$$

Note that the jet Reynolds number, defined as

$$Re_{jet} = \frac{\rho U_{jet} h}{\mu}, \tag{4.17}$$

is related to the chord Reynolds number, momentum coefficient and slot height-to-chord ratio:

$$C_\mu = 2\left(\frac{c}{h}\right)\left(\frac{Re_{jet}}{Re_c}\right)^2 = 2\left(\frac{h}{c}\right)\left(\frac{U_{jet}}{U_\infty}\right)^2. \tag{4.18}$$

Hence, only three of the following four parameters are independent: C_μ, Re_{jet}, Re_c and h/c. Therefore, the dimensionless length scales, such as y_{max}/c, and velocity scales, like U_{max}/U_∞, are dependent on the following parameters:

$$\frac{y_{max}}{c} = f\left(\frac{h}{c}, \frac{r}{c}, \frac{l}{c}, C_\mu, Re_c\right). \tag{4.19}$$

As noted earlier, r/c and l/c are constant in the present investigation. However, h/c, C_μ and Re_c are variable. Thus, two of these three parameters are kept constant, and the effect of varying the third parameter on y_{max} and other length and velocity scales is studied.

Table 6 summarizes the seven different cases that are included in this study of the curved wall jet. Cases 1–3 represent tests where Re_c and h/c are fixed, but C_μ changes. In cases 4 and 5, C_μ and h/c are fixed, but Re_c varies. Finally, in cases 4 and 6, C_μ and Re_c are fixed, but h/c differs. In the following sections, results from these six cases are presented and discussed. The seventh case is excluded from the initial analysis that follows but is used later as a 'test' case to check the validity of similarity parameter models.

4.3. *Flow characteristics*

Before studying the PIV measurements of the curved wall jet, the surface pressure distribution along the Coanda surface is examined. Note that the remainder of the
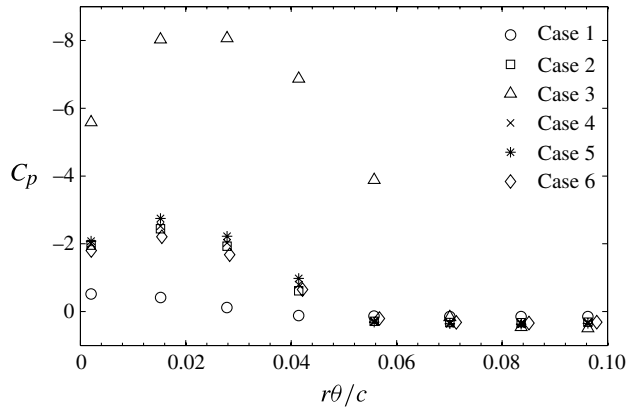
FIGURE 24. Coanda surface C_p. Refer to table 6 for test conditions for each case.

data presented are acquired in the open-jet test section configuration. Trailing-edge C_p data for the first six cases listed in table 6 are presented in figure 24. The data are plotted on an $r\theta/c$ axis based on the trailing-edge radius and the angular position relative to the slot exit plane (see figure 6). Initially, a favourable pressure gradient accelerates the flow for all cases except case 1 ($C_\mu = 0.0039$), where $U_{jet} \approx U_\infty$. Shortly thereafter, near $r\theta/c = 0.02$, a strong adverse pressure gradient develops. The trends displayed in figure 24 follow findings similar to those reported by Novak *et al.* (1987). Trailing-edge C_p provides insight into the expected similarity, or lack thereof, of the curved wall jet flow. In their study of a curved wall jet in the absence of an external flow, Neuendorf & Wygnanski (1999) observed full similarity of $\bar{U}$ (inner and outer regions) in the constant pressure region but only outer region similarity of $\bar{U}$ in the adverse pressure gradient region.

Profiles of mean velocity ($\bar{U}$ and $\bar{V}$), turbulence intensity ($(\overline{u'^2})^{1/2}$ and $(\overline{v'^2})^{1/2}$) and Reynolds stress ($\overline{u'v'}$) from PIV measurements along the rounded trailing edge are plotted in figure 25 at a variety of downstream distances from the slot for $Re_c = 6.5 \times 10^5$, $h/c = 0.0019$ and $C_\mu = 0.0039$, 0.015 and 0.057. Profiles for $C_\mu = 0.0039$ are not included when $r\theta/c > 0.040$ because separation occurs upstream of that position. Reliable PIV data are measured as close as 0.2 mm from the trailing-edge surface. The distance from the surface is normalized using the slot height h, and the flow quantities are normalized using the appropriate power of the jet velocity U_{jet}. Uncertainty bounds are removed from the plots for clarity. The mean tangential velocity profiles reveal how the jet decays and spreads as it travels away from the slot. As $\bar{U}$ decays, the mean normal velocity $\bar{V}$ increases and separation is approached. The turbulence intensities and Reynolds stress are significant in the immediate vicinity of the blunt slot lip and the high-shear region that exists there. As the jet spreads and entrains fluid from the external flow, the Reynolds stress becomes non-negligible over a growing region of the trailing edge. The similarity of the measured curved wall jet flow is assessed in the following section.

4.4. *Flow similarity*

Novak & Cornelius (1986) and Novak *et al.* (1987) showed that the outer region of $\bar{U}$ along the trailing edge of their circulation control aerofoil exhibited similarity when normalized using the scales suggested by Launder & Rodi (1983), which are
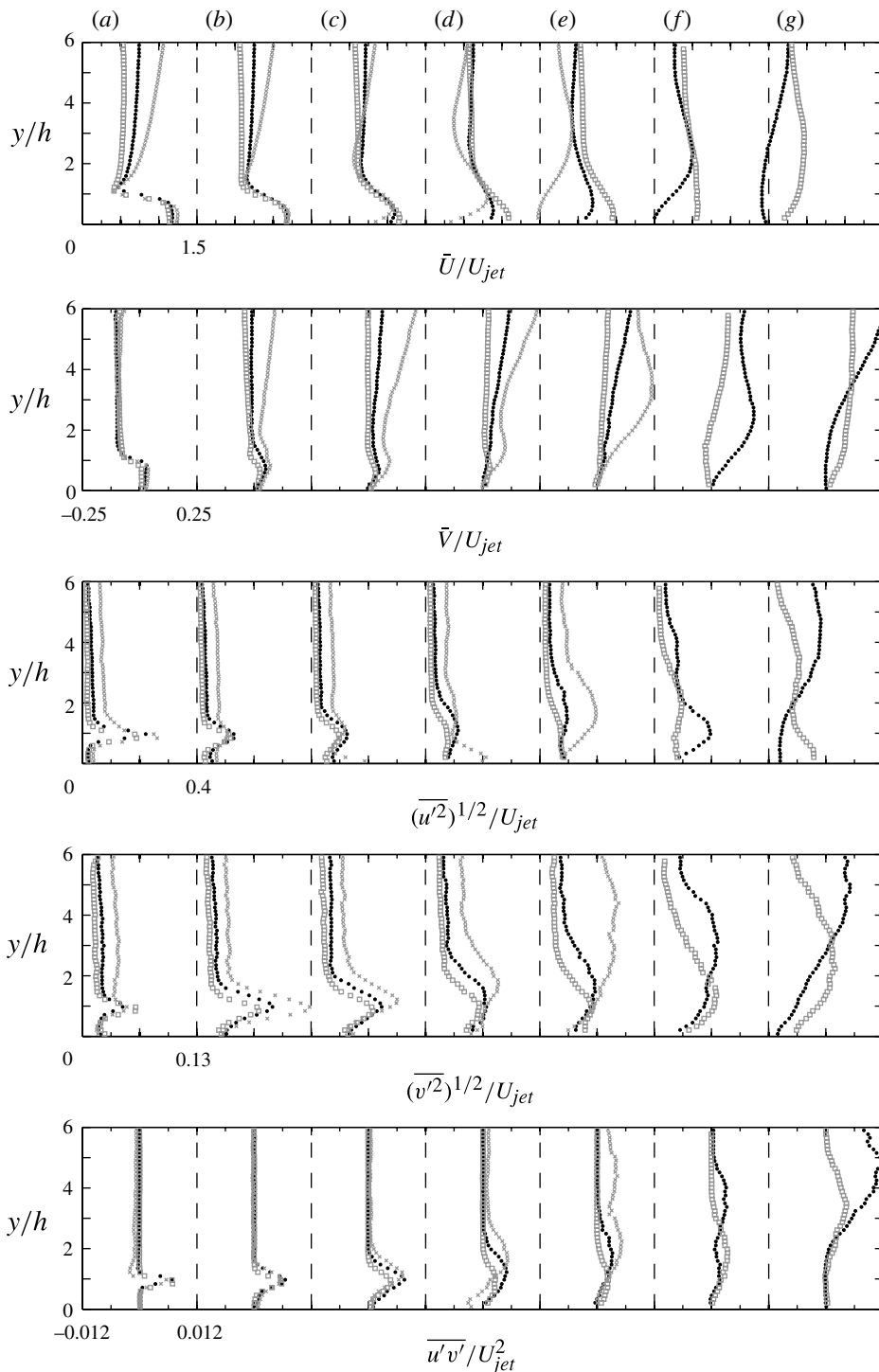
FIGURE 25. Circulation control curved wall jet profiles, $Re_c = 6.5 \times 10^5$, $h/c = 0.0019$ for various $r\theta/c$: (a) 0.0036, (b) 0.011, (c) 0.018, (d) 0.026, (e) 0.033 (f) 0.040 and (g) 0.048; $\times$, $C_\mu = 0.0039$; $\bullet$, $C_\mu = 0.015$; $\square$, $C_\mu = 0.057$. Note that the horizontal axis limits repeat across each panel.
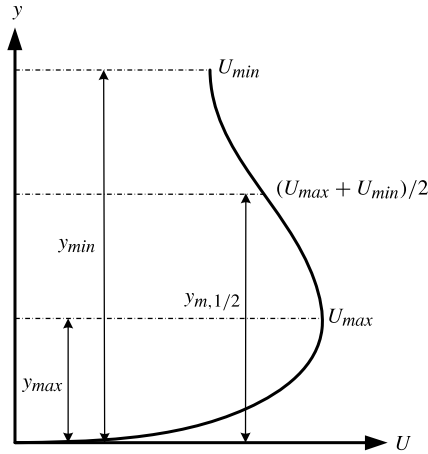
FIGURE 26. Length and velocity scales based on zero shear.

	Flow scales			
Authors	U_1	U_2	y_1	y_2
Launder & Rodi (1983)	U_e	U_{max}	$y_{e,1/2}$	y_{max}
Zhou & Wygnanski (1993)	U_∞	U_{max}	$y_{m/2}$	y_{max}
Present authors	U_{min}	U_{max}	$y_{m,1/2}$	y_{max}

TABLE 7. Comparison of flow scales suggested by Launder & Rodi (1983), Zhou & Wygnanski (1993) and the present authors (see figures 1 and 26).

restated in table 7 (also refer to figure 1). These same scales are applied to PIV data obtained in the open-jet test section in order to determine if similarity is achieved. In addition, the data are normalized using the scales found by Zhou & Wygnanski (1993) to collapse the outer region of $\bar{U}$ for a plane wall jet in an external flow. Those scales include local U_{max}, U_∞, y_{max} and $y_{m/2}$, which is the normal distance where $\bar{U} = U_{max}/2$. In the current set of experiments, the mean tangential velocity does not always decay to values of $U_{max}/2$. Hence, U_∞ is replaced with U_{min}, the velocity where the outer region mean shear approaches zero as described below, and $y_{m/2}$ is replaced with $y_{m,1/2}$, the normal distance where $\bar{U} = (U_{max} + U_{min})/2$. These scales are illustrated in figure 26 and listed in table 7. Note that the scales suggested by Zhou & Wygnanski (1993) and the present authors are potentially more practicable, since they do not require knowledge of the turbulence.

To normalize the mean tangential velocity profiles, the aforementioned length and velocity scales are first determined. The U_{max} value is found by detecting the point of maximum velocity on each mean tangential velocity profile, fitting a Gaussian curve to this point and its four nearest neighbours, and then computing the maximum of the curve fit. The scale y_{max} is simply the normal distance from the surface where $\bar{U} = U_{max}$. To determine U_{min} and y_{min}, first, the mean shear $(d\bar{U}/dy)$ is computed from the measured tangential velocity profile. Next, the two points on the mean shear
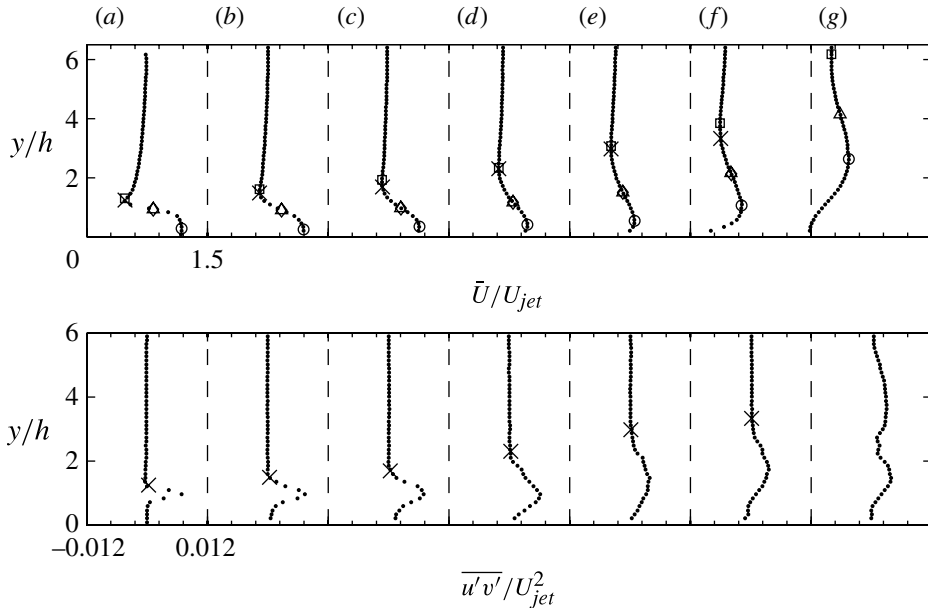
FIGURE 27. Circulation control curved wall jet profiles, $Re_c = 6.5 \times 10^5$, $C_\mu = 0.015$, $h/c = 0.0019$ for various $r\theta/c$: (*a*) 0.0027, (*b*) 0.010, (*c*) 0.017, (*d*) 0.025, (*e*) 0.032 (*f*) 0.040 and (*g*) 0.047. Length scales are indicated by: $\bigcirc$, y_{max}; $\square$, y_{min}; $\times$, y_e; $\triangle$, $y_{m,1/2}$; $\diamond$, $y_{e,1/2}$.

profile nearest to $d\bar{U}/dy = 0$ for $y > y_{max}$ are identified, and linear interpolation is used to compute the exact point where $d\bar{U}/dy = 0$. The normal distance from the surface to this point is y_{min}. In some instances, $d\bar{U}/dy < 0$ throughout the outer region. In those situations, y_{min} is specified as the first instance where $(h/U_{jet})d\bar{U}/dy < 4 \times 10^{-6}$ (i.e. $\bar{U}/U_{jet}$ changes by less than 6×10^{-4}, which is determined by inspection of the data). With y_{min} specified, U_{min} is found by evaluating a third-order polynomial fit of the mean tangential velocity data for the six data points closest to $y = y_{min}$. The value $U_{m,1/2}$ is simply the average of U_{max} and U_{min}; and $y_{m,1/2}$ is determined by evaluating a piecewise cubic interpolation of the mean tangential velocity profile for $y_{max} \leqslant y \leqslant y_{min}$ at $\bar{U} = U_{m,1/2}$. To determine y_e, first, $\overline{u'v'}_{max}$ is determined using a Gaussian fit of the Reynolds stress profile in the same manner as U_{max} is determined from a Gaussian fit of the mean tangential velocity profile. Then, the first instance where $\overline{u'v'}/(\overline{u'v'})_{max} < 0.05$ outwards from the position of maximum Reynolds stress is deemed the negligible Reynolds stress location (0.05 is also chosen by inspection; slightly higher thresholds do not significantly affect the results). The third-order polynomial fit of the mean tangential velocity data is then evaluated at $y = y_e$ to determine U_e. Lastly, $U_{e,1/2}$ is just the average of U_{max} and U_e; and $y_{e,1/2}$ is estimated by evaluating a piecewise cubic interpolation of the mean tangential velocity profile for $y_{max} \leqslant y \leqslant y_e$ at $\bar{U} = U_{e,1/2}$.

The length scales y_{max}, y_{min}, y_e, $y_{m,1/2}$ and $y_{e,1/2}$ are plotted with the mean tangential velocity and Reynolds stress profiles for case 2 ($Re_c = 6.5 \times 10^5$, $C_\mu = 0.015$, $h/c = 0.0019$) in figure 27. Profiles are provided from $r\theta/c = 0.0027$ until just past separation at $r\theta/c = 0.047$. As figure 27 attests, there is little difference between y_{min} and y_e and between $y_{m,1/2}$ and $y_{e,1/2}$. Note the double-peak character of the Reynolds stress plot beyond separation when $r\theta/c = 0.047$. It is not possible to define U_e or y_e
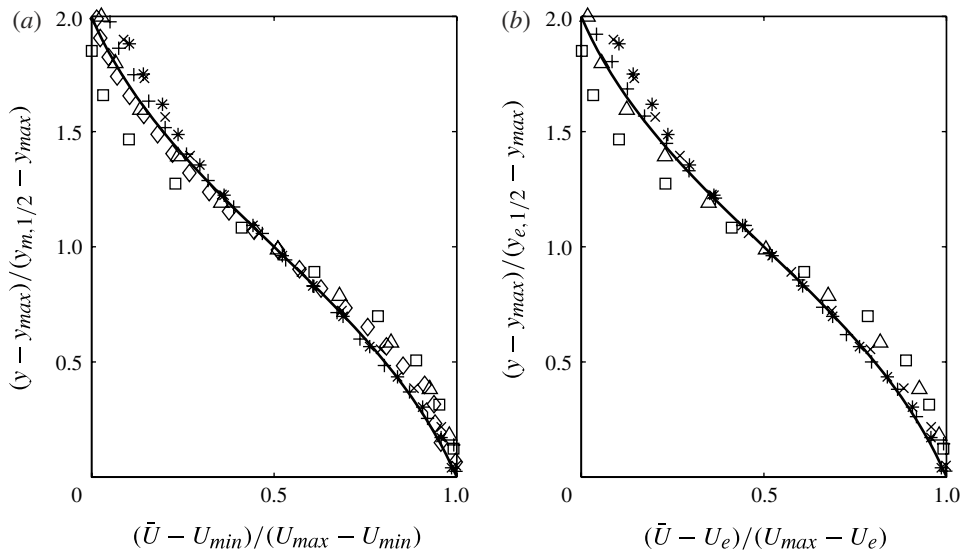
FIGURE 28. Outer region similarity of $\bar{U}$ using (*a*) mean shear scales and (*b*) scales suggested by Launder & Rodi (1983), $Re_c = 6.5 \times 10^5$, $C_\mu = 0.015$, $h/c = 0.0019$ for various $r\theta/c$: □, 0.010; △, 0.017; ×, 0.025; ∗, 0.032; +, 0.040; ◇, 0.047. The line represents $U^* = 0.5[1 - 1.315 \tanh(y^* - 1)]$. Mean squared errors for U^* are (*a*) 0.16 and (*b*) 0.068.

for this profile, so the scaling suggested by Launder & Rodi (1983) cannot be applied to these data.

The scales are used to normalize the outer regions of the mean tangential velocity profiles in figure 28, where it is seen that, using either the scaling suggested by Launder & Rodi (1983) or the modification to the approach by Zhou & Wygnanski (1993), the outer streamwise profiles exhibit similarity. Note that the velocity data at $r\theta/c = 0.0027$ are not included, as they do not collapse with the other profiles. In fact, only profiles in the constant pressure or adverse pressure gradient region along the trailing edge exhibit similarity, agreeing with the observations of Novak & Cornelius (1986), Novak *et al.* (1987) and Neuendorf & Wygnanski (1999). Furthermore, the $r\theta/c = 0.047$ data are not shown in figure 28(*b*), since U_e and y_e could not be defined for this profile. The solid line in figure 28 represents a hyperbolic tangent of the form

$$U^* = 0.5[1 - 1.315 \tanh(y^* - 1)], \qquad (4.20)$$

where U^* is the normalized velocity and y^* is the normalized distance from the surface.

Now that the outer region of $\bar{U}$ has been found to exhibit similarity, the inner region of $\bar{U}$ is studied. It is difficult to measure extremely close to the surface with PIV (recall that the slot height is typically 1 mm), so inner region data are limited compared to the outer region of the flow. Nevertheless, there are sufficient data to determine whether or not similarity is achieved. Inner region $\bar{U}$ data are normalized using y_{max} and U_{max} and plotted in figure 29. For clarity, profiles from additional $r\theta/c$ locations are included, and profiles near separation are excluded. Unlike the outer region, the inner region does not appear to exhibit similarity. These results agree with Neuendorf & Wygnanski (1999), who found that the inner region of $\bar{U}$ for a curved
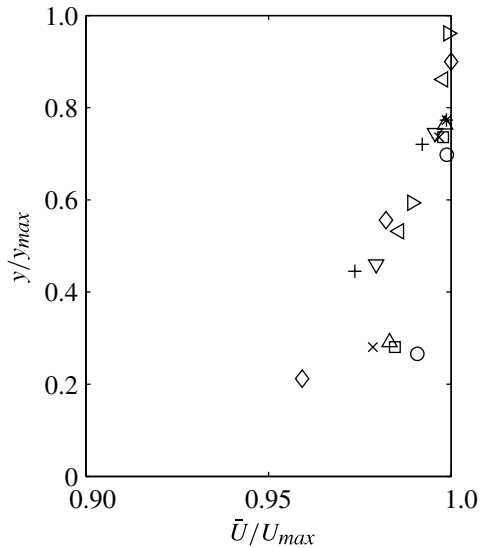
FIGURE 29. Lack of inner region similarity of $\bar{U}$, $Re_c = 6.5 \times 10^5$, $C_\mu = 0.015$, $h/c = 0.0019$ for various $r\theta/c$: $\circ$, 0.0027; $\square$, 0.0057; $\triangle$, 0.0087; $\times$, 0.012; $*$, 0.015; $\triangleright$, 0.018; $\diamond$, 0.021; $\triangleleft$, 0.024; $+$, 0.027; $\triangledown$, 0.030.

wall jet in quiescent surroundings does not exhibit similarity in the adverse pressure gradient region.

The remaining flow profiles, $\bar{V}$, $\overline{(u'^2)}^{1/2}$, $\overline{(v'^2)}^{1/2}$ and $\overline{u'v'}$, also do not exhibit similarity using any combination of mean velocity and length scales. In the following section, the evolution of the length and velocity scales found to collapse the outer region of $\bar{U}$ are analysed for the first six cases listed in table 6.

4.5. *Length and velocity scales*

The set of length and velocity scales based on the mean shear do not require knowledge of the flow turbulence and are thus more practicable in application than the scales suggested by Launder & Rodi (1983). As such, they are the focus of the remainder of the analysis. The length and velocity scales associated with this approach, y_{max}, $y_{m,1/2}$, U_{max} and U_{min}, are plotted in increments of $r\theta/c = 0.002$ for case 2 in figure 30. The data are plotted from just downstream of the slot exit to separation detected by the first sign of flow reversal. Figure 30 further illustrates the development and spread of the jet. The velocity scales initially increase, reach a maximum value near $r\theta/c = 0.015$, then decay at similar rates. The length scales y_{max} and $y_{m,1/2}$ are nearly constant initially, then increase gradually, and finally grow sharply as separation is approached. On the other hand, y_{min} increases immediately and then follows a parabolic form, similar to the other length scales.

For the first six test cases listed in table 6, the trends of y_{max}, $y_{m,1/2}$, U_{max} and U_{min} are analysed in an attempt to collapse each set of curves. Only data where the outer region exhibits similarity are included. Neuendorf & Wygnanski (1999) found that, for a curved wall jet in the absence of an external flow, the decay of U_{max} and the rate of spread of the jet described by the location where $U = U_{max}/2$ could be scaled using
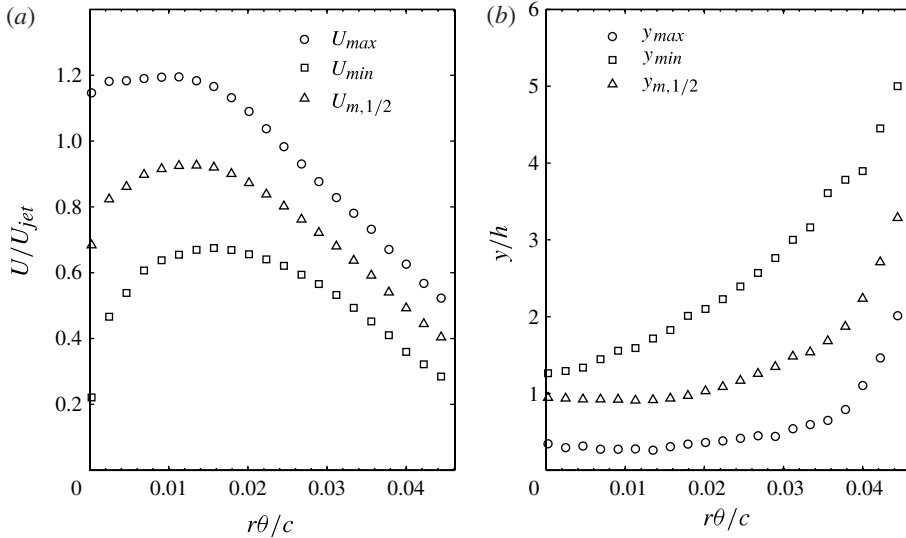
FIGURE 30. Velocity and length scales describing decay and spread of jet shown from just downstream of the slot exit to separation, $Re_c = 6.5 \times 10^5$, $C_\mu = 0.015$ and $h/c = 0.0019$.

the local kinematic jet momentum,

$$J = U_{max}^2 \, y_{m/2} \int_{y/y_{m/2}=0}^{\infty} \left(\frac{\bar{U}}{U_{max}} \right)^2 \mathrm{d} \left(\frac{y}{y_{m/2}} \right) = 0.78 U_{max}^2 \, y_{m/2}, \qquad (4.21)$$

and the wall radius in the constant pressure region. However, unlike the curved wall jet of Neuendorf & Wygnanski (1999), the entire velocity profile of the circulation control curved wall jet does not exhibit similarity. Hence, the local kinematic jet momentum cannot be expected to collapse the scales. Likewise, Neuendorf & Wygnanski observed that the rate of spread could be expressed solely as a function of the wall radius and downstream angular position from the slot. This is clearly not observed for the circulation control aerofoil, as shown in figures 31 and 32.

For a planar wall jet in an external flow, Zhou & Wygnanski (1993) found that the length and velocity scales describing the planar wall jet's spread and decay could be expressed as a function of a normalized downstream distance from the slot defined by XJ/ν^2, where X is the dimensional distance from the slot, ν is the kinematic viscosity and $J = h(U_{jet} - U_\infty)U_{jet}$ is the excess of kinematic momentum flux near the nozzle. A dimensionless velocity ratio $(U_{jet} - U_\infty)/(U_{jet} + U_\infty)$ was also used. These parameters do not collapse the current dataset either. Instead, the data are best fitted using Re_c, C_μ and h/c, as shown in figures 31–34. A power-law curve is fitted to each dataset by minimizing the square of the error. The scales, as a function of $r\theta/c$, are found to collapse with the product of Re_c and C_μ, referred to as the Reynolds-corrected momentum coefficient, which has recently been found to scale lift increments for active control of aerofoil flow separation (Stalnov *et al.* 2010). This scaling parameter takes into consideration the free stream boundary layer and its development as a function of Re_c. Recall figures 20 and 21, where, at higher values of C_μ, the mean tangential velocity profile of this upstream boundary layer actually resembles a wall jet more than a conventional boundary layer. The Reynolds-corrected momentum
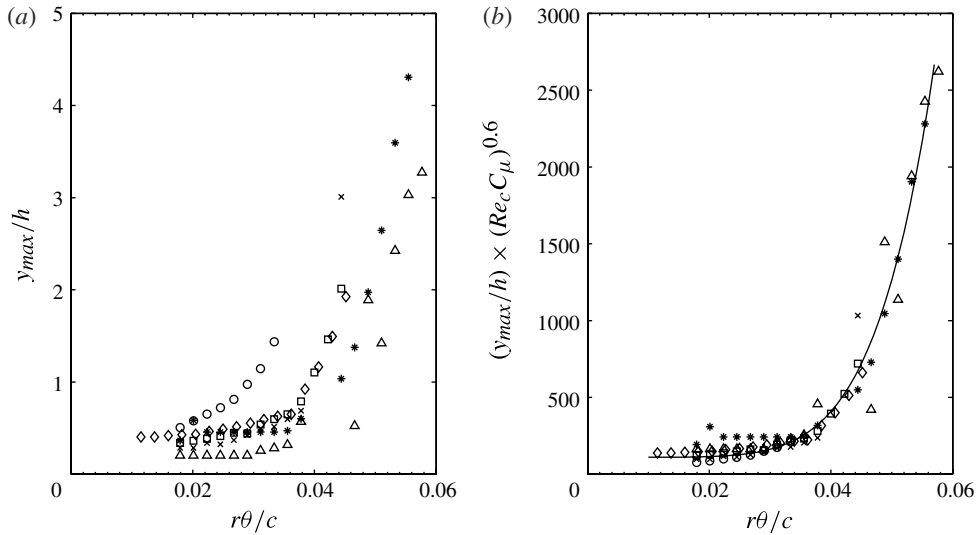
FIGURE 31. Rate of spread of y_{max}/h and collapsed data with best-fitting line, $R^2 = 0.95$. See table 6 for test conditions: $\circ$, case 1; $\square$, case 2; $\triangle$, case 3; $\times$, case 4; $*$, case 5; $\diamond$, case 6.

coefficient provides some basis to account for this effect. Best-fitted equations for the length and velocity scales are provided in (4.22)–(4.25):

$$\frac{y_{max}}{h} = \frac{1}{(Re_c C_\mu)^{0.60}} \left[9.0 \times 10^{10} \left(\frac{r\theta}{c} \right)^{6.1} + 110 \right], \tag{4.22}$$

$$\frac{y_{m,1/2}}{h} = 2.6 \times 10^{10} \left[\frac{1}{(Re_c C_\mu)^{0.11}} \frac{r\theta}{c} \right]^{5.7} + 1.0, \tag{4.23}$$

$$\left(\frac{U_{jet}}{U_{max}} \right)^2 = \left(\frac{h}{c} \right)^{-0.80} \left\{ 7.0 \times 10^6 \left[\frac{1}{(Re_c C_\mu)^{0.10}} \frac{r\theta}{c} \right]^{4.9} + 0.005 \right\}, \tag{4.24}$$

$$\left(\frac{U_{jet}}{U_{min}} \right)^2 = \left(\frac{h}{c} \right)^{-0.65} \left\{ 3.0 \times 10^{11} \left[\frac{1}{(Re_c C_\mu)^{0.18}} \frac{r\theta}{c} \right]^{5.9} + 0.04 \right\}. \tag{4.25}$$

Equations (4.22) and (4.23) reveal approximately a sixth-power dependence on the arc length $r\theta/c$. Contrast that to the results of the general similarity solution, which indicates that, for the self-similar flow over a logarithmic spiral surface, these scales should have a linear relationship with the arc length.

The product of the chord Reynolds number and momentum coefficient can also be rearranged as the product of the jet Reynolds number and jet-to-free stream velocity ratio:

$$Re_c C_\mu = \left(\frac{U_\infty c}{\nu} \right) \left[2 \left(\frac{h}{c} \right) \left(\frac{U_{jet}}{U_\infty} \right)^2 \right] = 2 \frac{U_{jet} h}{\nu} \frac{U_{jet}}{U_\infty} = 2 Re_{jet} \frac{U_{jet}}{U_\infty}. \tag{4.26}$$

Thus, in the case of the circulation control aerofoil, it appears that the rate of decay and spread of the jet are dependent on the jet Reynolds number. This is in contrast to the findings of Zhou & Wygnanski (1993), who determined that, as long
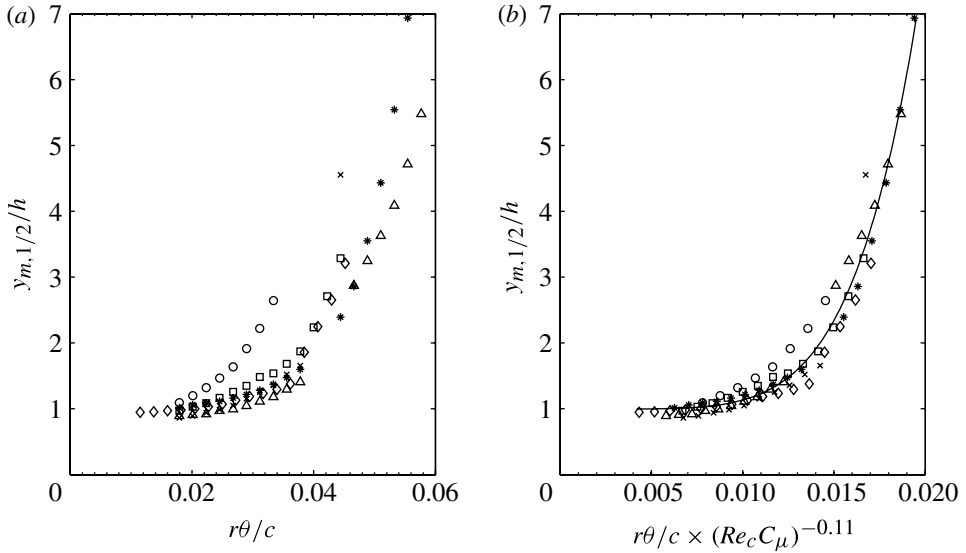
FIGURE 32. Rate of spread of $y_{m,1/2}/h$ and collapsed data with best-fitting line, $R^2 = 0.97$. See table 6 for test conditions: ∘, case 1; □, case 2; △, case 3; ×, case 4; ∗, case 5; ⋄, case 6.

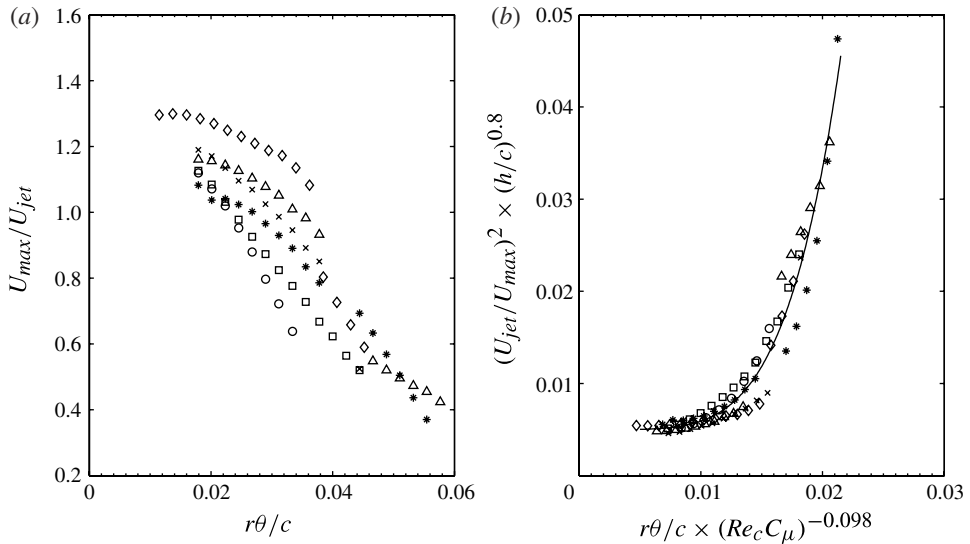
FIGURE 33. Rate of decay of U_{max}/U_{jet} and collapsed data with best-fitting line, $R^2 = 0.95$. See table 6 for test conditions: ∘, case 1; □, case 2; △, case 3; ×, case 4; ∗, case 5; ⋄, case 6.

as $U_{max}/U_\infty > 2$, the length and velocity scales describing the planar wall jet in an external flow are independent of the jet Reynolds number. Note that $U_{max}/U_\infty > 2$ for some profiles in cases 2–5 listed in table 6.

Equations (4.22) to (4.25) provide a predictive capability for the length and velocity scales of the mean outer region flow. Predicted and measured scales are compared in the next section.
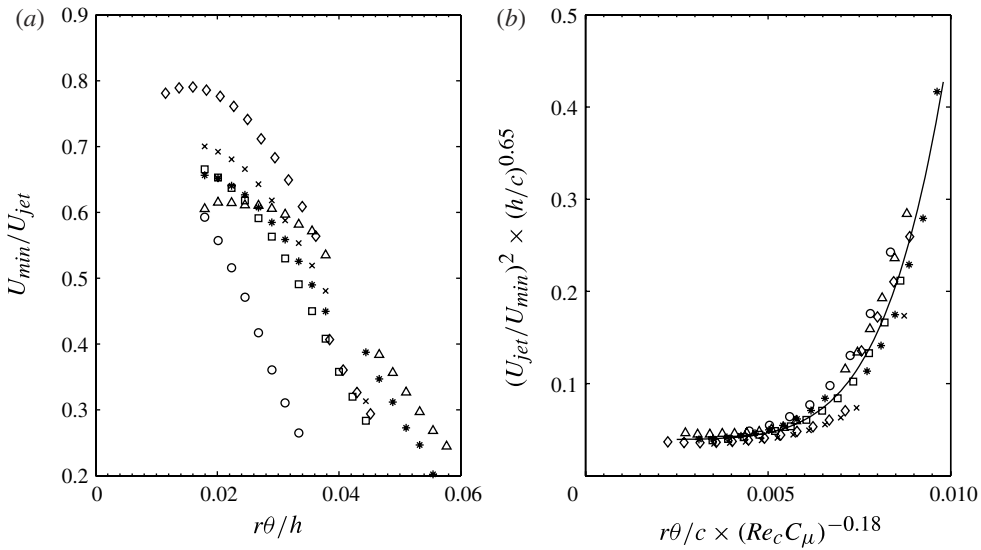
FIGURE 34. Rate of decay of U_{min}/U_{jet} for all cases listed in table 6, and collapsed data with best-fitting line, $R^2 = 0.95$. See table 6 for test conditions: ∘, case 1; □, case 2; △, case 3; ×, case 4; ∗, case 5; ◇, case 6.

FIGURE 35. Comparison of measured and predicted (*a*) velocity scales and (*b*) length scales, $Re_c = 6.5 \times 10^5$, $C_\mu = 0.015$, $h/c = 0.0019$. Measured scales are represented by symbols, and predicted scales are represented by lines.

4.6. *Flow prediction*

A comparison of the predicted and measured length and velocity scales is presented in figure 35 for $Re_c = 6.5 \times 10^5$, $C_\mu = 0.015$ and $h/c = 0.0019$. Overall, there is good agreement between the measured and predicted scales. The value of U_{min} is initially
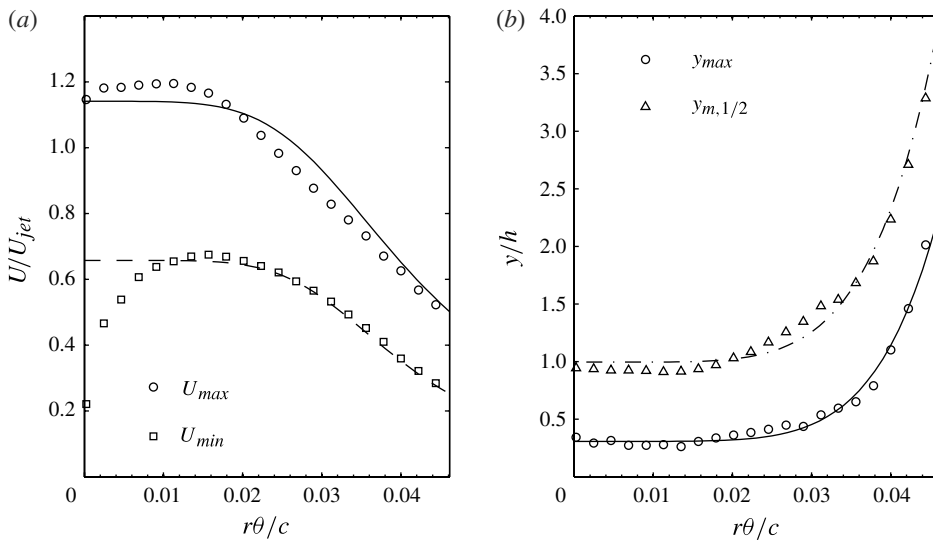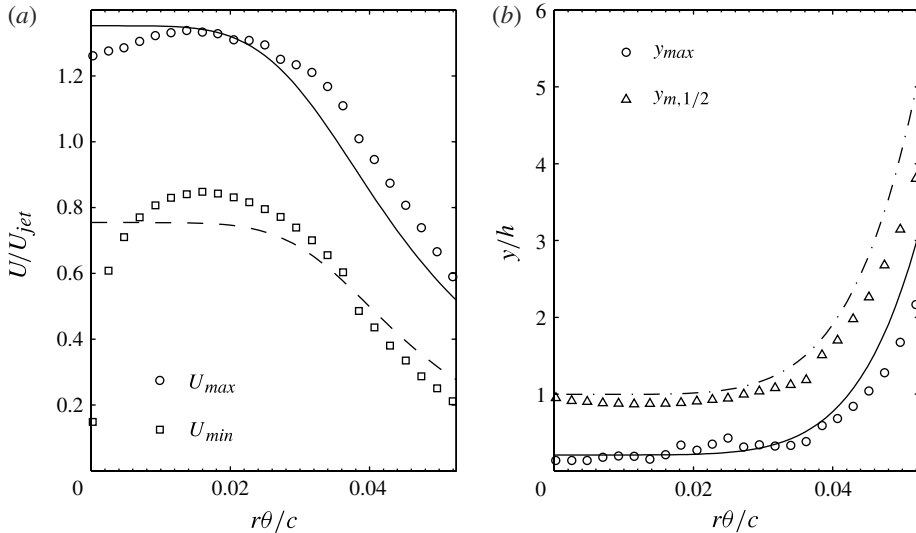
FIGURE 36. Comparison of measured and predicted (*a*) velocity scales and (*b*) length scales, $Re_c = 1.3 \times 10^6$, $C_\mu = 0.014$, $h/c = 0.0029$. Measured scales are represented by symbols, and predicted scales are represented by lines.

over-predicted in the favourable pressure gradient region; but recall that only data in the adverse pressure gradient region, where the outer region of $\bar{U}$ is similar, are used to determine (4.22)–(4.25). Despite that fact, the other scales are predicted reasonably well in the favourable pressure gradient region.

While the agreement between the predicted and measured flow fields in figure 35 is promising, it is a rather expected result since the data for those test conditions are used in determining the prediction equations. To truly test the prediction's capabilities, it should be compared to measurements for a case not included in the prior analysis. Thus, the predicted and measured scales are compared in figure 36 for case 7 in table 6 ($Re_c = 1.3 \times 10^6$, $C_\mu = 0.014$, $h/c = 0.0029$). Although there are larger differences between the predicted and measured scales in comparison with figure 35, the overall agreement is fair.

To this point, the curved wall jet flow has only been considered prior to separation. In the next section, flow separation is discussed.

5. Separation of the circulation control curved wall jet

It is well known that the circulation control curved wall jet is responsible for entraining free stream fluid, delaying separation and increasing circulation. The cause of separation is perhaps less clear and could be the result of a severe adverse pressure gradient (see figure 24), meandering streamwise vortices observed in curved wall jets in quiescent surroundings by Likhachev *et al.* (2001), Neuendorf *et al.* (2004) and Han *et al.* (2006), or a combination of influences.

Separation is studied in the present investigation by using PIV to measure the trailing-edge flow field and part of the wake region. Mean velocity magnitude contours and vectors are presented for $C_\mu = 0$, 0.014 and 0.057 in figure 37. When $C_\mu = 0$, a large wake is formed aft of the trailing edge, and the free stream flow appears symmetric about the chord line. With blowing, the flow along the upper surface of
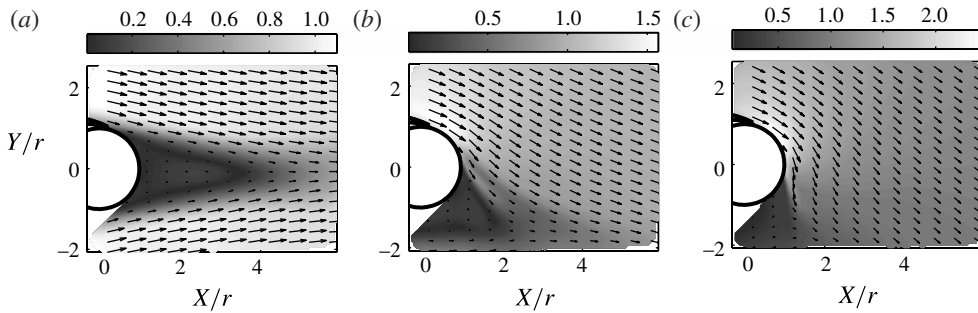
FIGURE 37. Mean velocity magnitude ($|V|/U_\infty$) contours and vectors, $Re_c = 6.5 \times 10^5$ and $h/c = 0.0019$. The aerofoil trailing edge is sketched for reference. (*a*) $C_\mu = 0$. (*b*) Upper slot blowing, $C_\mu = 0.014$. (*c*) Upper slot blowing, $C_\mu = 0.057$.
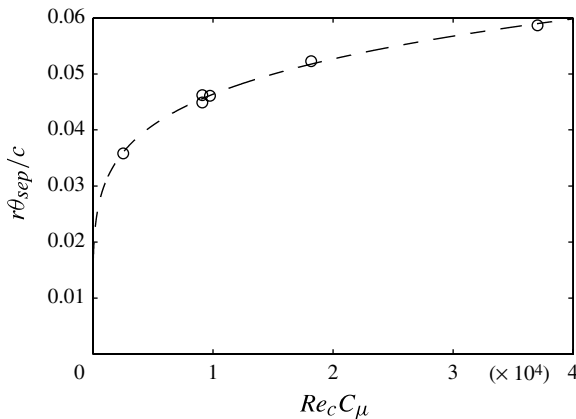

FIGURE 38. Approximate separation location as a function of $Re_c C_\mu$: ○, measured; – – –, fit ($R^2 = 0.996$).

the aerofoil remains attached and separates much farther downstream, as shown in figure 37(*b*). The vectors reveal the extent of flow turning due to entrainment from the jet. As C_μ further increases to 0.057 in figure 37(*c*), the free stream flow is deflected even more, and the separation point is shifted farther away from the blowing slot.

Figure 37 provides only a qualitative description of flow separation. For a more quantitative analysis, the curved wall jet PIV data are used to estimate the separation location by detecting the onset of flow reversal near the surface. Data along the trailing-edge surface are analysed in increments of 0.13 mm, which corresponds to the vector resolution of the dataset. Also, since it is not possible to resolve the flow field at the surface using PIV, the separation locations presented are only regarded as estimates, and the true separation locations probably occur just upstream of the estimated locations. The separation locations for the first six test cases listed in table 6 are plotted as a function of $Re_c C_\mu$ in figure 38, which indicates that the separation location moves farther downstream from the slot as the product of the chord Reynolds number and momentum coefficient increases. In particular, as $Re_c C_\mu$ initially increases, the separation distance increases at a high rate, but, at larger values of $Re_c C_\mu$, a

significant increase in the product of the two parameters yields only a small delay in separation. A curve, whose equation is given by

$$\frac{r\theta_{sep}}{c} = 0.0085(Re_c C_\mu)^{0.184}, \tag{5.1}$$

is fitted to these data so the separation distance can be estimated for a given Reynolds-corrected momentum coefficient. Equation (5.1) accurately predicts the estimated separation locations for both cases considered in § 4.6 (cases 2 and 7) with an error of less than $r\theta/c = 0.001$. Note that (5.1) is only applicable when $Re_c > 0$ and $C_\mu > 0$. With no external flow, the curved wall jet separates well downstream of the blowing slot when $Re_{jet} > 0$.

It should be noted that (5.1) may be applicable only to the aerofoil geometry of the present investigation and others like Abramson (1975). The separation locations reported by Novak & Cornelius (1986) and Novak *et al.* (1987) are under-predicted by between $r\theta/c = 0.04$ and 0.07 (for just one of their three datasets published, $Re_c C_\mu < 4 \times 10^4$, and the error is the smallest for that case). However, the trailing-edge geometry of the circulation control aerofoil studied by Novak and his colleagues is significantly different from the trailing edge of the circulation control aerofoil in the present investigation.

6. Summary and conclusions

Circulation control is a promising technology for improving underwater vehicle manoeuvrability. However, Howe (2002) cautioned that a circulation control aerofoil could be significantly louder than a conventional trailing edge, as additional noise sources are introduced by the interaction of the turbulent boundary layer and turbulent jet with the trailing-edge geometry. Tests are conducted on an elliptic circulation control aerofoil in an anechoic wind tunnel to support an effort to validate Howe's model and investigate trailing-edge flow similarity. Midspan surface pressure measurements obtained in the open-jet UFAFF test section reveal the absence of a leading-edge suction peak regularly observed in circulation control experiments and numerical studies. The lack of a leading-edge suction peak contributes to a lift reduction compared with prior tests of the same geometry in closed-wall test section wind tunnels. The leading-edge suction peak and corresponding lost lift are recovered by enclosing the wind tunnel test section. It is noted that the leading-edge surface pressure distribution is highly dependent on the boundary conditions enforced on the suction side of the aerofoil and the tunnel blockage ratio. Measured surface pressure distributions are compared with potential flow theory for flow around an ellipse using the conformal mapping technique. The theory provides insight into the behaviour of the flow and explains the elevated suction-side and reduced pressure-side surface pressure magnitudes measured with a rigid versus porous suction-side tunnel boundary. In addition, the theory also supports the observations that the pressure-side tunnel boundary is less important in determining the surface pressure distribution. This is perhaps counterintuitive, since one may expect the deflection of the jet towards and jet impingement on the pressure-side boundary (a phenomenon that has been observed during these experiments) to alter the pressure-side distribution.

PIV measurements reveal the extent to which enclosing the test section significantly modifies the leading-edge flow field. In an open-jet test section, leading-edge stagnation point movement is minimal with increasing momentum coefficient. In a closed-wall test section, leading-edge stagnation point movement is considerably

more significant as the momentum coefficient increases. Despite this behaviour, PIV measurements reveal negligible differences in the boundary-layer flow passing over the slot lip when the test section is opened or closed. Therefore, according to the theory of Howe (2002), the sound produced by the scattering of turbulent pressure fluctuations in this boundary layer off the slot lip should remain unchanged regardless of whether the test section is enclosed or not. This finding can provide direction to future researchers considering circulation control experiments in open-jet or closed-wall wind tunnels when acoustic measurements may be of interest.

Additional PIV measurements focus on the curved wall jet flow and its similarity. Although a similarity solution indicates that full flow similarity is only possible if the curved surface takes the impracticable shape of a logarithmic spiral, the outer regions of the mean tangential velocity profiles exhibit similarity using scales based on the maximum velocity and the Reynolds stress or mean shear (Launder & Rodi 1983; Zhou & Wygnanski 1993). The length and velocity scales required for similarity are measured for a collection of test cases where the chord Reynolds number, momentum coefficient and slot height vary. The data for these scales are assembled and found to provide reasonable collapse, and the resultant best-fitting equations of the dimensionless data are a function of the product of the chord Reynolds number and momentum coefficient. This so-called Reynolds-corrected momentum coefficient, proposed by Stalnov *et al.* (2010), can also be recast as a product of the jet Reynolds number and jet-to-free stream velocity ratio (see (4.26)). This indicates that, unlike the case of the planar wall jet in an external flow, the length and velocity scales describing the curved wall jet in an external flow are dependent on the jet Reynolds number (Zhou & Wygnanski 1993). The equations for predicting these length and velocity scales, given by (4.22)–(4.25), compare favourably with measurements.

Flow separation is also assessed using PIV, and, like the length and velocity scales of the flow, the separation location is a function of the Reynolds-corrected momentum coefficient. An equation for predicting the separation location is provided and found to match the present measurements with excellent accuracy. However, the equation may only be valid for the aerofoil geometry investigated, as using it to predict the separation location for a different geometry studied by Novak & Cornelius (1986) and Novak *et al.* (1987) leads to significant differences.

Acknowledgements

Appendix. Potential lifting flow over an ellipse

Potential lifting flow over a cylinder in a free stream is transformed to flow over an ellipse via conformal mapping (Katz & Plotkin 2001; Panton 2005). Consider the $z = x + \mathrm{i}y$ plane whose origin is located at the centre of a cylinder of radius R. The η plane, whose origin is located at the centre of the ellipse, is defined by

$$\eta = z + \frac{a^2}{z}, \tag{A 1}$$

where a is the transformation constant written in terms of the cylinder radius R, the ellipse semi-major axis A and the ellipse semi-minor axis B:

$$a = \sqrt{\tfrac{1}{2}R(A - B)}, \tag{A 2}$$

$$R = \tfrac{1}{2}(A + B). \tag{A 3}$$

The complex potential for lifting flow around a cylinder of radius R is the summation of the potentials for a uniform free stream, a doublet and a vortex:

$$F(z) = U_\infty \left(z + \frac{R^2}{z} \right) + \frac{i\Gamma \ln z}{2\pi}. \tag{A 4}$$

Taking the derivative of (A 4) yields the complex velocity,

$$W(z) = \frac{dF}{dz} = U_\infty \left(1 - \frac{R^2}{z^2} \right) + \frac{i\Gamma}{2\pi z}. \tag{A 5}$$

To determine the surface pressure on an ellipse with circulation in a free stream, the complex velocity $W(z)$ must be transformed to $W(\eta)$ using the conformal mapping function given by (A 1). Thus, it follows that

$$W(\eta) = \frac{dF}{d\eta} = \frac{dF}{dz}\frac{dz}{d\eta} = \frac{dF}{dz}\frac{1}{\dfrac{d\eta}{dz}}, \tag{A 6}$$

and the complex velocity on the ellipse surface, where $z = Re^{i\theta}$, is given by

$$W(\eta) = \frac{U_\infty(e^{i2\theta} - 1) + \dfrac{i\Gamma}{2\pi R}e^{i\theta}}{e^{i2\theta} - \dfrac{a^2}{R^2}}. \tag{A 7}$$

Since $W(\eta) = u - iv$, the magnitude of the velocity on the surface and hence the C_p distribution along the surface of the ellipse can be computed:

$$C_p = 1 - \left(\frac{|V_s|}{U_\infty} \right)^2 = 1 - \frac{u^2 + v^2}{U_\infty^2}. \tag{A 8}$$

The aforementioned analysis is extended to include rigid boundaries, like ground and ceiling planes, using the method of images (Katz & Plotkin 2001). Consider potential lifting flow around a circular cylinder placed a distance h_c from a ceiling plane, as shown in figure 39. An 'image' cylinder with circulation of opposite sense from the real cylinder is 'placed' a distance h_c from the opposite side of the plane. The origin of the real cylinder coincides with the origin of the $z_1 = x_1 + iy_1$ plane, and the origin of the image cylinder coincides with the origin of the $z_2 = x_2 + iy_2$ plane, which is offset from the z_1 plane such that $z_2 = z_1 - i2h_c$. The mapping transformation for the real cylinder is $\eta_1 = z_1 + a^2/z_1$, and the mapping transformation for the image cylinder is $\eta_2 = z_2 + a^2/z_2$. The complex potentials for the real and imaginary cylinders
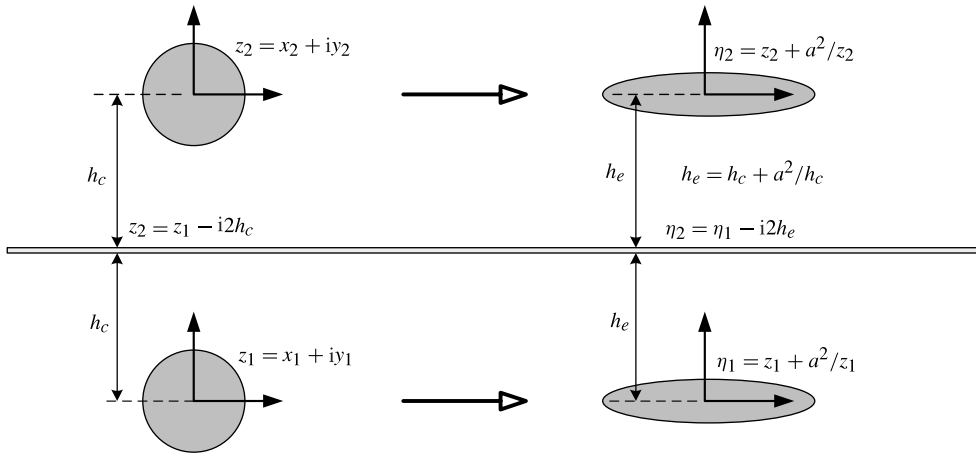
FIGURE 39. Method of images applied to lifting flow over an ellipse.

are given by the following equations:

$$F_1(z_1) = U_\infty \left(z_1 + \frac{R^2}{z_1} \right) + \frac{i\Gamma}{2\pi} \ln z_1, \tag{A 9}$$

$$F_2(z_2) = \frac{U_\infty R^2}{z_2} - \frac{i\Gamma}{2\pi} \ln z_2. \tag{A 10}$$

An expression is desired for the complex velocity of the flow around both ellipses as a function of η_1. For the real ellipse, this is straightforward and follows the steps outlined in the free stream flow analysis, giving

$$W_1(\eta_1) = \frac{\mathrm{d}F_1}{\mathrm{d}z_1} \frac{\mathrm{d}z_1}{\mathrm{d}\eta_1} = \left[U_\infty \left(1 - \frac{R^2}{z_1^2} \right) + \frac{i\Gamma}{2\pi z_1} \right] \frac{1}{1 - \dfrac{a^2}{z_1^2}}. \tag{A 11}$$

The complex velocity for the image ellipse is

$$W_2(\eta_1) = \frac{\mathrm{d}F_2}{\mathrm{d}z_2} \frac{\mathrm{d}z_2}{\mathrm{d}\eta_2} \frac{\mathrm{d}\eta_2}{\mathrm{d}\eta_1}. \tag{A 12}$$

The distance between the cylinders and the distance between the ellipses are not the same, since

$$h_e = h_c + \frac{a^2}{h_c}. \tag{A 13}$$

Therefore, $\eta_2 = \eta_1 - 2ih_e$, $\mathrm{d}\eta_2/\mathrm{d}\eta_1 = 1$, and the complex velocity for the image ellipse is given by

$$W_2(\eta_1) = - \left(\frac{U_\infty R^2}{z_2^2} + \frac{i\Gamma}{2\pi z_2} \right) \frac{1}{1 - \dfrac{a^2}{z_2^2}}. \tag{A 14}$$

Substituting $z_2 = z_1 - 2ih_c$ and then writing both complex velocities in terms of $z_1 = Re^{i\theta}$ yields the following complex velocities:

$$W_1(\eta_1) = \frac{U_\infty(e^{i2\theta} - 1) + \dfrac{i\Gamma}{2\pi R}e^{i\theta}}{e^{i2\theta} - \dfrac{a^2}{R^2}}, \tag{A 15}$$

$$W_2(\eta_1) = -\frac{1}{1 - \dfrac{a^2}{(Re^{i\theta} - 2ih_c)^2}}\left[\frac{U_\infty R^2}{(Re^{i\theta} - 2ih_c)^2} + \frac{i\Gamma}{2\pi(Re^{i\theta} - 2ih_c)}\right]. \tag{A 16}$$

Finally, the complex velocity on the surface of the real ellipse is just the superposition of the image and real ellipse complex velocities,

$$W(\eta_1) = W_1(\eta_1) + W_2(\eta_1). \tag{A 17}$$

Again, C_p is computed using (A 8).

If a ground plane is present instead of a ceiling plane, then the only change to the previous analysis is that $z_2 = z_1 + 2ih_c$ and $\eta_2 = \eta_1 + 2ih_e$. The presence of both ground and ceiling planes is accounted for by an infinite number of image ellipses, since each image itself is reflected by the additional plane (Katz & Plotkin 2001). Thus, the complex velocity on the surface of the real ellipse between two planes is given by the following summation:

$$\begin{aligned}
W(\eta_1) = {} & \frac{U_\infty(e^{i2\theta} - 1) + \dfrac{i\Gamma}{2\pi R}e^{i\theta}}{e^{i2\theta} - \dfrac{a^2}{R^2}} \\
& - \sum_{n=1}^{\infty} \frac{1}{1 - \dfrac{a^2}{(Re^{i\theta} - 2nih_c)^2}}\left[\frac{U_\infty R^2}{(Re^{i\theta} - 2nih_c)^2} + \frac{(-1)^{n+1}i\Gamma}{2\pi(Re^{i\theta} - 2nih_c)}\right] \\
& - \sum_{n=1}^{\infty} \frac{1}{1 - \dfrac{a^2}{(Re^{i\theta} + 2nih_c)^2}}\left[\frac{U_\infty R^2}{(Re^{i\theta} + 2nih_c)^2} + \frac{(-1)^{n+1}i\Gamma}{2\pi(Re^{i\theta} + 2nih_c)}\right]. \tag{A 18}
\end{aligned}$$

For moderate circulation, the lift coefficient computed from the results of (A 18) converges to within three significant digits with well under 500 image ellipses considered. However, this result is largely dependent on the specified circulation, as convergence is established with as few as 20 images for certain lift values.

REFERENCES

ABRAMSON, J. 1975 Two-dimensional subsonic wind tunnel evaluation of a 20-percent-thick circulation control aerofoil. *Tech. Rep.* ASED-331. DTNSRDC.

ABRAMSON, J. 1977 Two-dimensional subsonic wind tunnel evaluation of two related cambered 15-percent-thick circulation control aerofoils. *Tech. Rep.* ASED-373. DTNSRDC.

ABRAMSON, J. 2004 Characteristics of a cambered circulation control aerofoil having both upper and lower surface trailing edge slots. *Tech. Rep.* NSWCCD-50-TR-2004/030. NSWCCD.

BENEDICT, L. H. & GOULD, R. D. 1996 Towards better uncertainty estimates for turbulence statistics. *Exp. Fluids* **22** (2), 129–136.

COANDA, H. 1938 Propelling device. US Patent No. 2,108,652.

COLEMAN, H. W. & STEELE, W. G. 2009 *Experimentation, Validation, and Uncertainty Analysis for Engineers*, 3rd edn. John Wiley & Sons.

DAVIS, 2010 LaVision, ver. 7.4 (software package).

DAY, T. R. 2006 Coanda effect and circulation control for nonaeronautical applications. In *Applications of Circulation Control Technology* (ed. R. D. Joslin & G. S. Jones), pp. 599–614. AIAA.

ENGLAR, R. J. 1971 Two-dimensional subsonic wind tunnel tests of two 15-percent thick circulation control aerofoils. *Tech. Rep.* AL-211. NSRDC.

ENGLAR, R. J. 1975 Circulation control for high lift and drag generation on STOL aircraft. *J. Aircraft* **12** (5), 457–463.

ENGLAR, R. J. 2006 Pneumatic aerodynamic technology to improve performance and control of automotive vehicles. In *Applications of Circulation Control Technology* (ed. R. D. Joslin & G. S. Jones), pp. 357–382. AIAA.

GAETA, R. J., ENGLAR, R. J. & BLAYLOCK, G. 2006 Aerodynamic heat exchanger: a novel approach to radiator design using circulation control. In *Applications of Circulation Control Technology* (ed. R. D. Joslin & G. S. Jones), pp. 383–398. AIAA.

GRIFFIN, J., SCHULTZ, T., HOLMAN, R., UKEILEY, L. & CATTAFESTA, L. 2010 Application of multivariate outlier detection to fluid velocity measurements. *Exp. Fluids* **49** (1), 305–317.

GUITTON, D. E. & NEWMAN, B. G. 1977 Self-preserving turbulent wall jets over convex surfaces. *J. Fluid Mech.* **81** (1), 155–185.

HAN, G., DE ZHOU, M. & WYGNANSKI, I. 2006 On streamwise vortices and their role in the development of a curved wall jet. *Phys. Fluids* **18** (9) 095104.

HOWE, M. S. 2002 Noise generated by a Coanda wall jet circulation control device. *J. Sound Vib.* **249** (4), 679–700.

KATZ, J. & PLOTKIN, A. 2001 *Low-Speed Aerodynamics*, 2nd edn. Cambridge University Press.

KIND, R. J. & MAULL, D. J. 1968 An experimental investigation of a low-speed circulation-controlled aerofoil. *Aeronaut. Q.* **19**, 170–182.

KOBAYASHI, R. & FUJISAWA, N. 1983 Curvature effects on two-dimensional turbulent wall jets. *Arch. Appl. Mech.* **53** (6), 409–417.

LAUNDER, B. E. & RODI, W. 1983 The turbulent wall jet – measurements and modelling. *Annu. Rev. Fluid Mech.* **15**, 429–459.

LIKHACHEV, O., NEUENDORF, R. & WYGNANSKI, I. 2001 On streamwise vortices in a turbulent wall jet that flows over a convex surface. *Phys. Fluids* **13** (6), 1822–1825.

MATHEW, J., BAHR, C., CARROLL, B., SHEPLAK, M. & CATTAFESTA, L. 2005 Design, fabrication, and characterization of an anechoic wind tunnel facility. *AIAA Paper* 2005-3052.

MELLING, A. 1997 Tracer particles and seeding for particle image velocimetry. *Meas. Sci. Technol.* **8**, 1406–1416.

MURRAY, N. E. & UKEILEY, L. S. 2007 An application of gappy POD for subsonic cavity flow PIV data. *Exp. Fluids* **42**, 79–91.

NEUENDORF, R., LOURENCO, L. & WYGNANSKI, I. 2004 On large streamwise structures in a wall jet flowing over a circular cylinder. *Phys. Fluids* **16** (7), 2158–2169.

NEUENDORF, R. & WYGNANSKI, I. 1999 On a turbulent wall jet flowing over a circular cylinder. *J. Fluid Mech.* **381**, 1–25.

NEWMAN, B. G. 1961 The deflexion of plane jets by adjacent boundaries - Coanda effect. In *Boundary Layer and Flow Control: Its Principles and Applications,* Vol. 1 (ed. GUSTAV Victor Lachmann), pp. 232–262. Pergamon.

NOVAK, C. J. & CORNELIUS, K. C. 1986 An LDV investigation of a circulation control aerofoil flow field. *AIAA Paper* 1986-0503.

NOVAK, C. J., CORNELIUS, K. C. & ROADS, R. K. 1987 Experimental investigations of the circular wall jet on a circulation control aerofoil. *AIAA Paper* 1987-0155.

PANTON, R. L 2005 *Incompressible Flow*, 3rd edn. John Wiley & Sons.

POPE, A. & RAE, W. H. 1984 *Low-Speed Wind Tunnel Testing*. Wiley-Interscience.

REW, H. S. & PARK, S. O. 1988 The interaction of two opposing, asymmetric curved wall jets. *Exp. Fluids* **6** (4), 243–252.

ROGERS, E. O. & DONNELLY, M. J. 2004 Characteristics of a dual-slotted circulation control wing of low aspect ratio intended for naval hydrodynamic applications. *AIAA Paper* 2004-1244.

STALNOV, O., KRIBUS, A. & SEIFERT, A. 2010 Evaluation of active flow control applied to wind turbine blade section. *J. Renew. Sustain. Energy* **2** (6)063101.

WESTERWEEL, J. 1994 Efficient detection of spurious vectors in particle image velocimetry data sets. *Exp. Fluids* **16** (3-4), 236–247.

WETZEL, D. 2011 An experimental investigation of circulation control acoustics. PhD thesis, University of Florida.

WETZEL, D., GRIFFIN, J., LIU, F. & CATTAFESTA, L. 2009 An experimental study of circulation control on an elliptic aerofoil. *AIAA Paper* 2009-4280.

WETZEL, D., GRIFFIN, J., LIU, F. & CATTAFESTA, L. 2010 An experimental study of a circulation control aerofoil trailing edge flow field. *AIAA Paper* 2010-4576.

WETZEL, D., LIU, F. & CATTAFESTA, L. 2012 A theoretical and experimental study of broadband circulation control noise. *AIAA Paper* 2012-2061.

WILLIAMS, R. M. 1969 Some research on rotor circulation control. In *Proceedings of the 3rd Cal/AV LABS Symposium*.

WILLIAMS, R. M. & HOWE, H. J. 1970 Two-dimensional subsonic wind tunnel tests on a 20 percent thick, 5 percent cambered circulation control aerofoil. *Tech. Rep.* AL-176. NSRDC.

WILSON, D. J. & GOLDSTEIN, R. J. 1976 Turbulent wall jets with cylindrical streamwise surface curvature. *Trans. ASME: J. Fluid Engng* **98**, 550–557.

ZHOU, M. D. & WYGNANSKI, I. 1993 Parameters governing the turbulent wall jet in an external stream. *AIAA J.* **31** (5).